

The weak Fe fluorescence line and long-term X-ray evolution of the Compton-thick active galactic nucleus in NGC 7674

P. Gandhi,^{1,2★} A. Annuar,² G. B. Lansbury,^{2,3} D. Stern,⁴ D. M. Alexander,²
F. E. Bauer,^{5,6,7} S. Bianchi,⁸ S. E. Boggs,⁹ P. G. Boorman,¹ W. N. Brandt,^{10,11,12}
M. Brightman,¹³ F. E. Christensen,¹⁴ A. Comastri,¹⁵ W. W. Craig,^{14,16} A. Del Moro,¹⁷
M. Elvis,¹⁸ M. Guainazzi,^{19,20} C. J. Hailey,²¹ F. A. Harrison,¹³ M. Koss,²²
I. Lamperti,²² G. Malaguti,²³ A. Masini,^{15,24} G. Matt,⁸ S. Puccetti,^{25,26} C. Ricci,⁵
E. Rivers,¹³ D. J. Walton^{3,4,13} and W. W. Zhang²⁷

Affiliations are listed at the end of the paper

Accepted 2017 February 8. Received 2017 February 7; in original form 2016 May 24

ABSTRACT

We present *NuSTAR* X-ray observations of the active galactic nucleus (AGN) in NGC 7674. The source shows a flat X-ray spectrum, suggesting that it is obscured by Compton-thick gas columns. Based upon long-term flux dimming, previous work suggested the alternate possibility that the source is a recently switched-off AGN with the observed X-rays being the lagged echo from the torus. Our high-quality data show the source to be reflection-dominated in hard X-rays, but with a relatively weak neutral Fe $K\alpha$ emission line (equivalent width [EW] of ≈ 0.4 keV) and a strong Fe $xxvi$ ionized line (EW ≈ 0.2 keV). We construct an updated long-term X-ray light curve of NGC 7674 and find that the observed 2–10 keV flux has remained constant for the past ≈ 20 yr, following a high-flux state probed by *Ginga*. Light travel time arguments constrain the minimum radius of the reflector to be ~ 3.2 pc under the switched-off AGN scenario, ≈ 30 times larger than the expected dust sublimation radius, rendering this possibility unlikely. A patchy Compton-thick AGN (CTAGN) solution is plausible, requiring a minimum line-of-sight column density (N_H) of 3×10^{24} cm $^{-2}$ at present, and yields an intrinsic 2–10 keV luminosity of $(3\text{--}5) \times 10^{43}$ erg s $^{-1}$. Realistic uncertainties span the range of $\approx (1\text{--}13) \times 10^{43}$ erg s $^{-1}$. The source has one of the weakest fluorescence lines amongst bona fide CTAGN, and is potentially a local analogue of bolometrically luminous systems showing complex neutral and ionized Fe emission. It exemplifies the difficulty of identification and proper characterization of distant CTAGN based on the strength of the neutral Fe $K\alpha$ line.

Key words: galaxies: Seyfert – X-rays: individual (NGC 7674).

1 INTRODUCTION

Obscured active galactic nuclei (AGN) dominate the overall population of AGN in the cosmos, especially the efficiently accreting sources that power the cosmic hard X-ray background radiation (e.g. Setti & Woltjer 1989; Comastri et al. 1995; Gandhi & Fabian 2003; Gilli, Comastri & Hasinger 2007; Treister, Urry & Virani 2009; Ballantyne et al. 2011; Ueda et al. 2014). Yet, finding and characterizing these objects is made difficult by the strong absorption they can suffer across the electromagnetic spectrum. In particular, the census of the sources hidden behind extreme obscuring column

densities of gas – in particular, Compton-thick AGN with column densities $N_H \gtrsim 1.5 \times 10^{24}$ cm $^{-2}$, hereafter CTAGN – remains highly incomplete (see Ricci et al. 2015 and Koss et al. 2016 for recent updates on the hard X-ray-selected CTAGN census). Even locally, very few robust (bona fide) CTAGN are known (Della Ceca et al. 2008; Goulding et al. 2012; Gandhi et al. 2014).

One candidate of a nearby, luminous CTAGN is NGC 7674, the brightest member of the Hickson 96 interacting galaxy group. NGC 7674 is a known Seyfert 2, showing strong narrow optical emission lines with full width at half-maximum (FWHM) of less than 500 km s $^{-1}$ in spectral observations carried out over three decades ago (Feldman et al. 1982). The source also shows a prolific outflow, which manifests as a prominent shoulder on the blue wings of all the prominent narrow optical lines. The outflow has been

* E-mail: p.gandhi@soton.ac.uk

studied in detail using *Hubble Space Telescope* spectroscopy by Fischer et al. (2013), who find blueshifts of up to $\sim 1700 \text{ km s}^{-1}$ (and even larger FWHM) along the narrow-line region aligned with the jet axis of the source. In the radio, NGC 7674 shows at least three separate compact components in very long baseline interferometry (VLBI) observations on scales of ≈ 0.7 arcsec corresponding to ≈ 0.4 kpc, and there have been suggestions that the collimated ejecta associated with the radio source could also drive the optical-emitting line outflow (Unger et al. 1988). Even higher resolution VLBI observations by Momjian et al. (2003) reveal a complex ‘S’-shaped structure, which could result from interactions of the jet with the interstellar medium. Using the [O III] emission line as a bolometric luminosity indicator, Xu, Livio & Baum (1999) classify NGC 7674 as a radio-quiet AGN.

The source was first reported to be a reflection-dominated AGN by Malaguti et al. (1998) from *BeppoSAX* X-ray observations carried out in 1996, with the direct (intrinsic) continuum being fully absorbed by a Compton-thick gas column. *BeppoSAX* detected NGC 7674 over the energy range of ~ 0.1 –60 keV. Malaguti et al. reported a complex structure to the neutral Fe $K\alpha$ line, and estimated a high intrinsic AGN luminosity assuming a scattering geometry similar to NGC 1068. But the *BeppoSAX* observation was not the first X-ray observation of the source. As detailed in a historical X-ray analysis by Bianchi et al. (2005), the source was likely detected by the *HEAO* mission in the late 1970s at a 2–10 keV flux level almost 30 times brighter (Grossan 1992) and subsequently with an intermediate flux by *Ginga* (Awaki et al. 1991). Bianchi et al. (2005) discuss several potential caveats to these detections, including *HEAO* contamination by nearby sources, and systematic uncertainties related to the background level measured by *Ginga*, and conclude that the combined weight of evidence favours the historical source detections being real, although the *Ginga* flux measurement is considered to be more reliable of the two, due to a more robust background determination. The *Ginga* spectrum is a lightly absorbed power law (PL, with $N_{\text{H}} < 2 \times 10^{22} \text{ cm}^{-2}$) with an upper limit of 80 eV to the equivalent width (EW) of any neutral Fe $K\alpha$ emission line. The source then declined by an order of magnitude in continuum flux by the time it was observed by *BeppoSAX* to be Compton-thick. Such behaviour might argue for the source being a member of the class of ‘changing-look’ AGN (e.g. Matt, Guainazzi & Maiolino 2003), associated with clumps of obscuring clouds transiting across the line of sight (los) resulting in apparent changes in $N_{\text{H}}(\text{los})$. The most famous example of this class is NGC 1365 that shows dramatic N_{H} variability on time-scales of days (Risaliti et al. 2005).

However, an *XMM-Newton* observation carried out 6 yr later (in 2004) also showed a reflection-dominated spectrum completely consistent in shape as well as flux with *BeppoSAX*, unlike what may be expected in a changing-look AGN. Bianchi et al. (2005) interpret the source as potentially having switched-off, with the spectrum observed by *BeppoSAX* and *XMM-Newton* being the reflection component that is delayed with respect to the direct, illuminating PL. Another source that has been discussed from these two opposing perspectives recently is NGC 7582 (Rivers et al. 2015). Bianchi et al. (2005) also found a relatively weak Fe $K\alpha$ emission line in NGC 7674, possibly blended with an ionized Fe xxvi line at 6.97 keV.

Approximately 10 yr after the last *XMM-Newton* observation, NGC 7674 was observed by *Suzaku* in 2013 and then by *NuSTAR* in 2014, in addition to several snapshot observations by the *Swift* satellite between 2011 and 2014. Here, we present a spectral analysis of these unpublished observations, and combine this with historical data to study the long-term source evolution. We discuss and

Table 1. Observation log.

Mission	Instrument(s)	Observation date	Exposure (ks)
<i>NuSTAR</i>	FPMA/B	2014-09-30	52.0/51.9
<i>Suzaku</i>	XIS0/1/3	2013-12-08	52.2/52.2/52.2
<i>Swift</i>	XRT	2011-01-28...2014-10-08 ^a	48.8 ^a

^a For *Swift*, 17 observations are combined here. See Appendix A for details.

place constraints on the switched-off AGN as well as the CTAGN scenarios. Finally, we touch upon the relevance of the complex Fe lines for the identification and characterization of distant CTAGN. We assume $H_0 = 67.3 \text{ km s}^{-1} \text{ Mpc}^{-1}$ and $\Omega_{\Lambda} = 0.685$ (Planck Collaboration XVI 2014), corresponding to a distance of 126 Mpc corrected to the reference frame defined by the cosmic microwave background. The source systemic redshift is $z = 0.0289$. All X-ray spectral fitting is carried out with the *XSPEC* package v12.9.0 (Arnaud 1996) and uncertainties are quoted at 90 per cent confidence, unless stated otherwise.

2 OBSERVATIONS

A log of the *NuSTAR*, *Suzaku* and *Swift* X-ray observations analysed herein is presented in Table 1, and the individual data sets are described in this section.

2.1 NuSTAR

NGC 7674 was observed by *NuSTAR* (Harrison et al. 2013) for about 52 ks of exposure on 2014 September 30 (ObsID 708023010). *NuSTAR* is the first orbiting telescope capable of focusing X-rays above ~ 10 keV, operating over the energy range of 3–79 keV. The data were processed using standard steps and the *NuSTAR* Data Analysis Software (NUSTARDAS) v.1.3.0 that is provided as part of HEASOFT¹ and associated FTOOLS (Blackburn 1995). *NuSTAR* CALDB calibration files were used to generate cleaned event files after filtering for South Atlantic Anomaly passages and the standard depth cut, in order to reduce instrumental background.

Source spectra were extracted using a circular aperture 45 arcsec in radius centred on the source position in both focal plane modules (FPMs). Background spectra were extracted from source-free regions on the detector. The *nuproducts* task was used to extract these calibrated spectra and to generate corresponding response files. All spectra were grouped to a minimum signal to noise of at least 4 per grouped energy bin after background subtraction for fitting purposes.

The source is well detected in both FPMs with 3–78 keV count rates per second of 2.92 ± 0.08 (FPMA) and 2.53 ± 0.08 (FPMB).

2.2 Suzaku

About 52 ks of exposure were obtained on 2013 December 08 with *Suzaku*. The X-ray Imaging Spectrometer (XIS; Koyama et al. 2007) is sensitive over ≈ 0.5 –10 keV. Standard FTOOLS software for *Suzaku* was used for data reduction and cleaned event file generation with recommended filtering. Source counts were extracted from within a 3.4 arcmin radius aperture for integrating XIS source counts, and

¹ <https://heasarc.gsfc.nasa.gov>

background counts from a larger source-free polygon. The generated spectra and responses of the two front-illuminated (FI) detectors were combined together, and this was analysed simultaneously with the back-illuminated (BI) detector data. For the fitting, we ignore the energy ranges of 1.7–1.9 and 2.1–2.3 keV because of calibration uncertainties.

The source was also observed by the Hard X-ray Detector (HXD; Kokubun et al. 2007; Takahashi et al. 2007). The HXD/PIN data (the PIN array is sensitive between ≈ 15 and 60 keV) were reduced using standard tasks. The `FTOOLS` routine `hxdpinxbpi` is a pipeline task that first extracts spectral counts and corrects these for deadtime. Using the ‘tuned’ background model for the target observation provided by the *Suzaku* team as a starting point (Fukazawa et al. 2009), `hxdpinxbpi` also outputs a background spectrum including the cosmic X-ray background component. However, after background subtraction, the residual source count rate was found to be 0.013 cts s^{-1} (15–60 keV), which is ≈ 5.0 per cent of the gross count rate and similar to the level of background reproducibility for observations after 2012.² We conservatively consider the source as a non-detection but note that fitting a PL to the detected net counts between 15 and 60 keV returns an observed flux $F_{15-60} \approx 5 \times 10^{-12} \text{ erg s}^{-1} \text{ cm}^{-2}$, which is similar to the observed *NuSTAR* flux in the same band with the best-fitting models that we will discuss in the Results section.

NGC 7674 is also too faint to be detectable in the HXD/Gadolinium Silicate Scintillator array sensitive to much higher energies, and those data are not considered here.

2.3 *Swift*

The source has been observed by *Swift* (Gehrels et al. 2004) on 17 occasions 2011 onwards, with exposure times ranging over ≈ 470 –5100 s using the X-Ray Telescope (XRT; Burrows et al. 2005) sensitive to photons between ~ 0.3 and 10 keV. The individual observations are listed in the Appendix A. We extracted source and background spectra, together with response files, using the standard XRT Data Analysis Software tools with `HEASOFT`. The version of `XRTPIPELINE` used was 0.13.0. Source counts were extracted within a 20 arcsec radius aperture, and background was extracted from an off-source sky region. Upper limits (for detection significance less than 10^{-3}) were estimated using the `SOSTA` command in the `XIMAGE` package.

We first analysed the spectra individually, but the source lies at the limit of detectability in these observations, yielding only weak detections for observations longer than 2 ks, and non-detections in other cases. Nevertheless, the individual observations (detections and limits) allow a first check for any strong variations with time. These fits are also described in Appendix A, and no significant variations are found.

We then extracted a co-added XRT spectrum by combining the event files of the individual observations. This yields a data set with a total exposure time of 48.8 ks. The source is well detected in this combined exposure, with a net count rate of $7.9 (\pm 0.4) \times 10^{-3} \text{ ct s}^{-1}$ over the energy range of 0.5–10 keV.

The source is classified as a non-detection by the Burst Alert Telescope (BAT; Barthelmy et al. 2005) sensitive over 14–195 keV using standard analysis adopted for the 70-month all-sky survey (Baumgartner et al. 2013), and we do not consider the BAT data

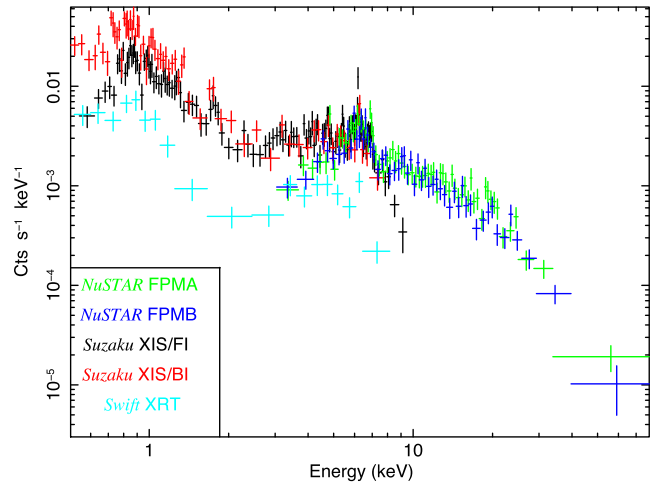


Figure 1. The *NuSTAR*, *Suzaku* and *Swift* data plotted in observed count rate units.

further in this work. We do note, however, that a custom analysis by Koss et al. (2013) finds a 4.2σ detection at the position of NGC 7674 with a flux $F_{14-195} = 9.9_{-2.4}^{+5.1} \times 10^{-12} \text{ erg s}^{-1} \text{ cm}^{-2}$, consistent with that inferred from our *NuSTAR* analysis described later.

2.4 Optical spectroscopy

In preparation for, and in support of, the *NuSTAR* observations, we also obtained optical spectroscopy of NGC 7674 using the Low Resolution Imaging Spectrometer (LRIS) on the Keck Telescope (Oke et al. 1995). The observations were carried out on 2014 June 25 through a 1.0 arcsec wide slit, using both the blue ($600 \text{ lines mm}^{-1}$) grism and the red ($400 \text{ lines mm}^{-1}$) grating, with the D560 dichroic. The night was photometric, with seeing close to 0.7 arcsec.

The blue spectral region is dominated by strong emission lines with blueshifted components, as reported in many previous works (e.g. Feldman et al. 1982). The red spectral region contains the isolated Ca II absorption triplet, which can be used to estimate the central black hole mass. This estimate is presented in Appendix A. The instrumental resolution in the red spectral region was measured to be 7.4 \AA (FWHM) using arc lamp spectra, corresponding to a velocity resolution of $\sigma_{\text{instr.}} = 107 \text{ km s}^{-1}$ close to the observed wavelength of the Ca triplet feature.

2.5 X-ray spectral analysis methodology

In this section, we start by checking for consistency of the data between the various missions, and then describe the details of the spectral analysis models.

2.5.1 Basic characterization

Fig. 1 shows the *NuSTAR*, *Suzaku* and *Swift* data sets overplotted in count rate units, stretching over two decades in observed energy from 0.5 to 78 keV. The spectral shape approximately matches between the missions and instruments over common energy ranges. In particular, there appears to be a broad hump dominating the *NuSTAR* band above 10 keV and a sharp emission feature around 6 keV. These are strongly reminiscent of reflection resulting from Compton scattering and neutral Fe fluorescence, a common characteristic of obscured AGN X-ray spectra. The hump extends down to ~ 3 keV in all data sets, below which a different component appears

² www.astro.isas.jaxa.jp/suzaku/analysis/hxd/pinxb/tuned/140530bgdd.pdf

to dominate in both the *Suzaku*/XIS and *Swift*/XRT data with the spectrum rising and peaking around 1 keV (this is related to the peak in the effective area, in the spectral units of Fig. 1).

Fitting a PL to the continuum over the common energy range of 3–10 keV (after ignoring the range of 5.5–7 keV around the neutral Fe $K\alpha$ line) simultaneously to all missions returns a photon index $\Gamma = 0.73 \pm 0.11$ with an acceptable fit statistic of $\chi^2/\text{dof} = 99.9/92$. This is much harder than the typical intrinsic photon indices ($\langle \Gamma \rangle \sim 1.9$) seen in AGN X-ray spectra (cf. Nandra et al. 1997; Mateos et al. 2005; Piconcelli et al. 2005) and is suggestive of heavy obscuration. Fitting the same model to the data from each mission separately, the observed 2–10 keV fluxes span the range of $F_{2-10} \approx (7-14) \times 10^{-13} \text{ erg s}^{-1} \text{ cm}^{-2}$ between the missions (with the harder *Swift* photon index giving the highest flux), and are fully consistent with each other at 90 per cent confidence.

We note a mild discrepancy in the *Swift* XRT data with respect to the other missions. When examining the individual photon indices in the above fit to each mission separately, we find $\Gamma_{\text{XRT}} = -0.68 \pm 1.26$. This is harder than the median Γ value from the other missions at 90 per cent confidence. But at 95 per cent confidence, we find that all missions do agree. The cause of this slight mismatch is not clear but is unlikely to be related to differing aperture sizes used for extracting spectra for the different missions, because we expect the unresolved AGN alone to be the dominant contributor at these energies. Instead, at soft energies, one may expect spatially extended emission and larger differences, which we will discuss later. In any case, since this discrepancy is relatively mild, and since all other observations are fully consistent with each other, we consider a joint analysis of the *NuSTAR*, *Suzaku* XIS and co-added *Swift* XRT data to be justified, and this is the approach we follow in the rest of this paper.

2.5.2 Reflection models

For the detailed spectral fits, we will be fitting X-ray reflection models over much of the hard X-ray energy range. There are several canonical models available for fitting heavily obscured AGN spectra in XSPEC. Traditionally, PEXRAV (Magdziarz & Zdziarski 1995) and its successor PEXMON including fluorescence (Nandra et al. 2007) have been used to characterize reflection features. These assume a slab obscurer/reflector with an infinite optical depth, as may be expected in a standard geometrically thin accretion disc. The incident source in X-rays is associated with PL radiation (PL_{AGN}) from a hot electron accretion disc corona. More recently, there are models that simulate X-ray processing in finite optical depth toroidal media, which are more physically appropriate for obscured AGN. Murphy & Yaqoob (2009) provide tabulated results of Monte Carlo simulations of an AGN illuminating a doughnut-shaped torus with a fixed opening angle and covering factor of 0.5 (the MYTORUS model). Brightman & Nandra (2011) assume, instead, a torus defined as a conical section of a sphere with variable opening angle and hence variable covering factor (the TORUS model). Both models assume Solar abundances and treat absorption, reflection and Fe $K\alpha$ fluorescence self-consistently. MYTORUS additionally allows the freedom to vary the parameters of the scatterer, the los obscurer, and the fluorescer, decoupled from one another. Both torus models assume that there is no e-folding cut-off energy to PL_{AGN} . For consistency, we make the same assumption in PEXMON. All models assume a uniform gas density spatial distribution.

Since the geometry of the obscuring/reflecting medium is unknown, we will use all three geometries above and investigate the range in intrinsic properties that can satisfy the observations.

2.5.3 Additional model components

Fixed Galactic absorption ($\text{PHABS}_{\text{Gal}}$) with $N_{\text{H}} = 4.27 \times 10^{20} \text{ cm}^{-2}$ (Dickey & Lockman 1990) was included in all models. We also included constants to account for cross-calibration uncertainties between the various detectors and missions. We found that one or two APEC (Smith et al. 2001) components and a soft power law (PL_{soft}) were required to represent the energy range below ~ 2 keV in some models. We emphasize that these components are meant to serve as parametrisations only. Previous works have shown that the origin of the soft X-ray photons in obscured AGN is a complex mixture of AGN photoionization, starburst emission and PL contributions from X-ray binaries (XRBs), among various possible origins (e.g. Sako et al. 2000; Kinkhabwala et al. 2002; Cappi et al. 2006; Guainazzi & Bianchi 2007). Separating these various possible components in NGC 7674 will require high- spatial and spectral resolution observations with *Chandra* and *Athena*, respectively. Our main focus is the origin of the higher energy X-rays, so we use the APEC and PL_{soft} components simply to ensure that the spectral fits over the soft regime are statistically acceptable. In addition, we may expect spatially extended soft emission to contribute in differing amounts to the *Suzaku* and *Swift* spectra because of the differing spectral extraction apertures tuned to the sizes of the respective telescope point spread functions. We account for this simply by allowing the APEC components to vary independently between these two missions. The only cross-check required in this regard is that the soft X-ray flux measured by *Swift* XRT (with the smaller aperture) should not exceed that observed in *Suzaku* XIS. This cross-check was applied post-fitting and found to hold for the best fits presented in the following sections.

With regard to other components, some models preferred several layers of absorption in addition to Galactic, as follows:

- (i) Nuclear obscuration: All models with a transmission component required a thick nuclear absorber, which we associate with the classical compact torus having an los column density ' $N_{\text{H}}(\text{nuc})$ ' well above 10^{24} cm^{-2} .
- (ii) Host galaxy absorption: Most models preferred the inclusion of a weak absorber screening the soft thermal and PL components (denoted by ' $N_{\text{H}}(\text{host})$ ' with values of a few times 10^{21} cm^{-2}). This corresponds to weak host galaxy reddening and is consistent with optical reddening of the narrow-line region, as we discuss later.
- (iii) Scattering screen: One alternative scenario that we will investigate requires an additional absorbed PL continuum component, which can potentially be attributed to scattering of the intrinsic PL_{AGN} into the los. The scattered fraction is f_{scatt} , i.e. $\text{PL}_{\text{scatt}} = f_{\text{scatt}} \times \text{PL}_{\text{AGN}}$. Absorption is required for this component, but as we will discuss later, the data cannot distinguish between the two possibilities of (1) a screen that absorbs only the scattered PL, and (2) a screen that affects all the compact nuclear components (direct, reflected, as well as scattered), with both possibilities allowed for in our analysis. We follow the more generic case (b) above, and term this component ' $N_{\text{H}}(\text{scatt})$.' It shows intermediate-column density values with $N_{\text{H}}(\text{scatt}) \sim 10^{23} \text{ cm}^{-2}$.

Finally, we found that inclusion of a hydrogen-like Fe XXVI line at 6.97 keV, probably related to the ionized scattered continuum, provided a significant improvement in all models. Our model values at any energy E can most generically be described as follows.

$$F(E) = C e^{-\tau(\text{Gal})} e^{-\tau(\text{host})} [\text{APEC}(s) + \text{PL}_{\text{soft}} + e^{-\tau(\text{scatt})} [\text{Torus}(\Gamma, N_{\text{H}}(\text{nuc})) + \text{PL}_{\text{scatt}}(\Gamma) + \text{Line}]],$$

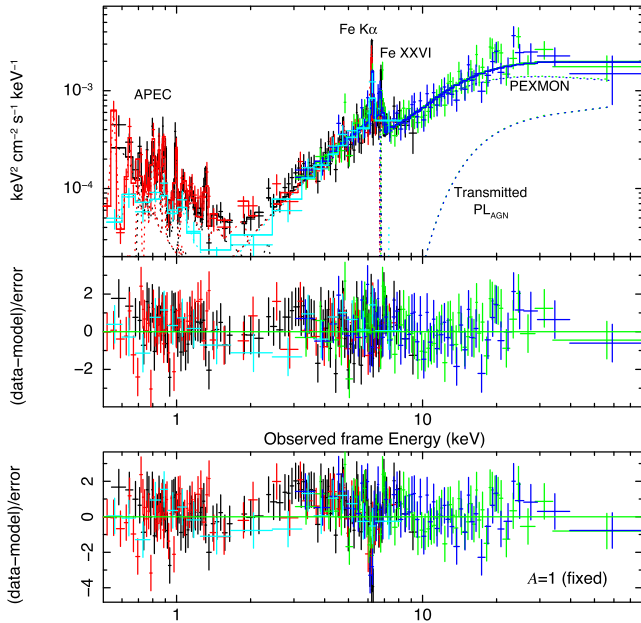


Figure 2. PEXMON model fit to the *Suzaku* XIS FI (black), XIS BI (red), *NuSTAR* FPMA (green), FPMB (blue) and *Swift* XRT (cyan) data. The central panel shows the fit residuals. The Fe abundance for this fit is close to 0.5 (Table 2). The bottom panel shows the residuals to a fit with fixed abundance $A = 1$. Note the strong overprediction at the neutral Fe $K\alpha$ energy.

where ‘Torus’ represents one of our three primary models including either (i) PEXMON (Model P), or (ii) Brightman & Nandra TORUS (Model T), or (iii) Murphy & Yaqoob MYTORUS (Model M), in order to model the primary nuclear obscurer and reflector with column density $N_{\text{H}}(\text{nuc})$. ‘C’ represents cross-calibration constants, τ is the optical depth $N_{\text{H}} \times \sigma(E_z)$ at the rest-frame energy E_z of the absorber, and ‘Line’ refers to the Fe XXVI emission line. We emphasize that not all models require the complexity implied by the above generic description of components.

3 RESULTS

3.1 Model P: PEXMON

We began with fitting Model P (PEXMON). This slab reflection model can fit the Compton hump successfully but strongly overpredicts the Fe $K\alpha$ line strength when using fixed abundances at the Solar value. Letting the elemental abundance ($A = A_{\text{Fe}}$) vary freely yields an acceptable solution ($\chi^2/\text{dof} = 324.7/305$) with $\Gamma = 2.1^{+0.2}_{-0.1}$, $A = 0.5 \pm 0.1$ and a slab inclination of at least 77° . The inclination affects the ‘peakiness’ of the Compton hump, with lower inclinations being too ‘peaky’ as compared to the data.³ This Model P solution is plotted in Fig. 2 and fit parameters are listed in Table 2. The bottom panel in the same figure demonstrates the strong Fe $K\alpha$ residuals with A fixed to Solar and $\Gamma = 2.1$ (fixed to the same value as the canonical Model P); letting Γ vary freely did not provide a better fit than that stated in Table 2.

A transmitted component of the direct AGN power law (PL_{AGN}) is included in this model. Compton scattering and photoelectric absorption by the torus are simulated with standard multiplicative models CABS and ZPHABS, respectively, with the gas column density

$N_{\text{H}}(\text{nuc})$ tied between the two models. The best-fitting $N_{\text{H}}(\text{nuc}) = 3.4^{+0.8}_{-0.6} \times 10^{24} \text{ cm}^{-2}$. The reflection component dominates the absorbed transmitted component over the entire spectral range probed, i.e. the source is fully reflection-dominated. The excess of the reflection component is a factor of ~ 3 around 30 keV. We note that excluding the transmission component results in a moderate increase in the fit statistic to $\chi^2/\text{dof} = 334.5/306$, which is only marginally significant at the 3σ level. In other words, a transmission component is not strongly required.

We find that the cross-calibration constants between the various missions are consistent with 1 within the uncertainties. The strength of the Fe XXVI line is $\text{EW}(\text{Fe XXVI}) \approx 200 \text{ eV}$. At the soft end, the *Suzaku* XIS data require two APEC components with temperatures $kT \approx 0.1$ and 0.6 keV, whereas the *Swift* XRT data probing smaller apertures require only a single lower temperature component. The APEC abundances are ~ 0.01 – 0.2 . Multiple thermal models with widely differing temperatures and abundances are quite common in luminous infrared galaxies (e.g. Ranalli et al. 2008) and have also been seen in other CTAGN (e.g. Konami et al. 2012). There is, however, strong degeneracy between the abundances and temperatures in data with low spatial and spectral resolution, and tying all the *Suzaku* and *Swift* model abundances to each other also yields an acceptable solution ($\chi^2/\text{dof} = 332/307$) with a global abundance $A = 0.27^{+0.56}_{-0.14}$, a *Swift* APEC₃ component temperature of $kT_3 = 0.19^{+0.03}_{-0.08} \text{ keV}$, and no significant changes to the corresponding temperatures for the APEC₁ and APEC₂ *Suzaku* components. However, we emphasize that we are not attempting to constrain the origin of the soft X-ray emission in detail here.

The best-fitting model needs only one additional layer of absorbing column density $N_{\text{H}}(\text{host}) = 4.0^{+2.1}_{-1.6} \times 10^{21} \text{ cm}^{-2}$. This is a rather thin screen and corresponds to an optical extinction $E_{B-V} = 0.7^{+0.4}_{-0.3} \text{ mag}$ for a standard Galactic gas-to-dust ratio (Bohlin, Savage & Drake 1978). This is consistent with the reddening expected from the Balmer decrement of 4.80 (Bassani et al. 1999). Removing this layer significantly worsens the fit to $\chi^2/\text{dof} = 342.1/306$. But most of the change is concentrated at the softest energies (resulting in an increased APEC temperature) that we are not modelling in detail; the primary AGN reflection component is unaffected.

3.2 Model T: TORUS

PEXMON assumes a slab geometry with infinite density, which is unlikely to be representative of the toroidal obscurer envisaged by AGN unification schemes. So we next turned to the Brightman & Nandra TORUS model. This also allows us to explore alternatives to our low A_{Fe} solution, because abundances are fixed at Solar values in this model. In this case, an acceptable solution may be found if we effectively dilute the continuum emission from the torus at the Fe $K\alpha$ line energy with a stronger scattered component (PL_{scatt}).⁴ Such a solution is plotted in Fig. 3, where $N_{\text{H}}(\text{nuc})$ is above 10^{25} cm^{-2} , well within the Compton-thick regime. The scattered fraction is $f_{\text{scatt}} \approx 4$ per cent, which raises the continuum at the Fe $K\alpha$ line energy sufficiently to produce a fully acceptable fit ($\chi^2/\text{dof} = 320.2/300$). For this fit, we froze the inclination angle θ_{inc} of the torus to be close to edge-on, as is recommended for exploration of the full range of possible covering factors (Brightman et al. 2015). There are uncertainties in the TORUS model at edge-on inclinations, as discussed by Liu & Li (2015). We checked that varying θ_{inc} did not

³ For an illustration of this effect, see fig. 5 of Magdziarz & Zdziarski (1995).

⁴ See the presentation by T. Yabooob at <http://cxc.cfa.harvard.edu/ChandraDecade/> for more discussions of such a warm scatterer scenario.

Table 2. Results of X-ray spectral fitting to NGC 7674.

Component	Parameter	Model P	Model T	Model M	Units
Primary absorber/reflector	$N_{\text{H}}(\text{nuc})$	$3.4^{+0.8}_{-0.6}$	36^{+u}_{-10}	$5.5^{+u}_{-2.3}$	10^{24} cm^{-2}
	$N_{\text{H}}(\text{eq})$	//	//	$10.0^{+u}_{-4.1}$	10^{24} cm^{-2}
	θ_{inc}	85^{+u}_{-8}	87.1^f	65^{+9}_{-4}	\circ
	θ_{tor}	–	62^{+15}_{-11}	–	\circ
	R	-1^f	–	–	
	A_{Fe}	$0.51^{+0.10}_{-0.11}$	$-‡$	$-‡$	
	EW(Fe $K\alpha$)	$0.38^{+0.10}_{-0.09}$	\dagger
EW(Fe xxvi)	$0.20^{+0.11}_{-0.09}$	\dagger	keV
PL _{AGN}	Γ	$2.07^{+0.15}_{-0.11}$	$1.80^{+0.15}_{-0.11}$	$1.93^{+0.28}_{-0.12}$	
Additional components					
Host absorption	$N_{\text{H}}(\text{host})$	$4.0^{+2.1}_{-1.6}$	$3.1^{+1.7}_{-1.1}$	$3.4^{+0.2}_{-0.2}$	10^{21} cm^{-2}
APEC ₁ ^a	kT_{apec1}	$0.11^{+0.03}_{-0.02}$	$0.12^{+0.03}_{-0.03}$	$0.11^{+0.04}_{-0.04}$	keV
	A_{apec1}	$0.1^{+u}_{-0.08}$	$0.1^{+0.6}_{-0.09}$	$0.1^{+0.8}_{-0.07}$	
APEC ₂ ^a	kT_{apec2}	$0.56^{+0.07}_{-0.07}$	$0.59^{+0.07}_{-0.07}$	$0.59^{+0.09}_{-0.08}$	keV
	A_{apec2}	$0.3^{+0.8}_{-0.1}$	$0.2^{+0.5}_{-0.1}$	$0.3^{+0.5}_{-0.2}$	
APEC ₃ ^a	kT_{apec3}	$0.17^{+0.05}_{-0.04}$	$0.15^{+0.06}_{-0.04}$	$0.14^{+0.06}_{-0.04}$	keV
	A_{apec3}	$0.01^{+0.07}_{-u}$	$0.01^{+0.11}_{-u}$	$0.01^{+0.16}_{-u}$	
PL _{soft}	Γ_{soft}	–	2.0^f	2.0^f	
	Norm	–	$2.5^{+1.2}_{-1.5}$	$2.5^{+1.4}_{-1.5}$	$10^{-5} \text{ ph keV}^{-1} \text{ cm}^{-2} \text{ s}^{-1}$
Scattering	f_{scatt}	–	3.5 ± 1.2	$6.1^{+3.6}_{-3.1}$	10^{-2}
	$N_{\text{H}}(\text{scatt})$	–	9.4 ± 2.5	$10.6^{+3.3}_{-2.3}$	10^{22} cm^{-2}
$C_{\text{XIS BI}}^{\text{cross-calib}}$	CONST	1.00 ± 0.07	1.01 ± 0.07	$1.00^{+0.07}_{-0.07}$	
$C_{\text{FPMA}}^{\text{cross-calib}}$	CONST	$1.06^{+0.08}_{-0.07}$	1.11 ± 0.08	$1.12^{+0.09}_{-0.08}$	
$C_{\text{FPMB}}^{\text{cross-calib}}$	CONST	$1.04^{+0.09}_{-0.07}$	$1.10^{+0.05}_{-0.08}$	$1.11^{+0.09}_{-0.09}$	
$C_{\text{XRT}}^{\text{cross-calib}}$	CONST	$0.98^{+0.13}_{-0.13}$	1.01 ± 0.14	$1.00^{+0.15}_{-0.14}$	
χ^2/dof		325/305	320/300	325/300	

Model P: PEXMON component fit (Nandra et al. 2007).

Model M: MYTORUS coupled component fit (Murphy & Yaquob 2009).

Model T: TORUS model component fit (Brightman & Nandra 2011).

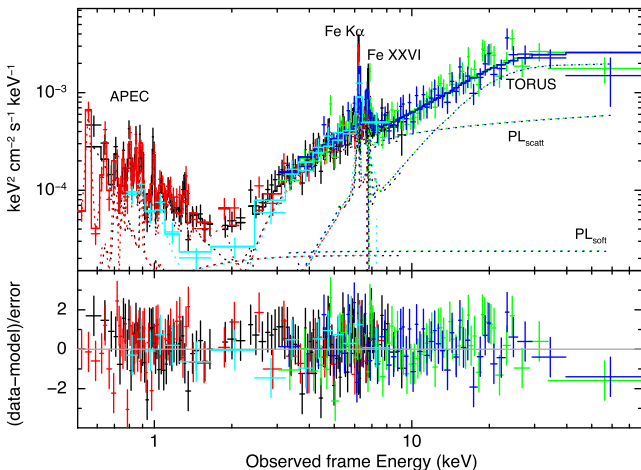
^uunconstrained to within the model limits. N_{H} upper limits are 10^{25} and 10^{26} cm^{-2} for MYTORUS and TORUS, respectively. APEC is defined between abundances of 0 to 5, relative to Solar.

^ffixed.

[†]Equivalent width measured using a simple Gaussian atop a locally fitted power-law continuum.

^a APEC₁ and APEC₂ represent thermal components in *Suzaku* XIS, and APEC₃ is for *Swift* XRT.

[‡]These models are defined for abundances fixed to Solar only.


Figure 3. *Suzaku*, *Swift* and *NuSTAR* data fits with the reflection Model T. Colours are as in Fig. 2.

affect our final inferences. The best-fitting opening angle is $\theta_{\text{tor}} = 62^{+15}_{-11} \circ$. Smaller opening angles produce a worse fit because they result in Compton humps peakier than required by the data.⁵ Large values of θ_{tor} are allowed up to $\theta_{\text{tor}} = 77^\circ$, beyond which the torus effectively becomes too geometrically thin to produce a sufficiently strong Compton hump.

In this model, however, an additional intermediate column obscurer $N_{\text{H}}(\text{scatt}) \sim 10^{23} \text{ cm}^{-2}$ is required, so as not to overproduce the soft X-ray flux. We note that in our model configuration, $N_{\text{H}}(\text{scatt})$ affects PL_{scatt} as well as the compact nuclear TORUS component. But modifying the model such that $N_{\text{H}}(\text{scatt})$ affects PL(scatt) alone also yields a fully acceptable solution with $\chi^2/\text{dof} = 323.3/300$. This consistency results from the fact that PL_{scatt} completely dominates over the TORUS reflection continuum at energies of

⁵ See fig. 1 of Brightman et al. (2015) for an illustration of the effect of changing θ_{tor} .

around a few keV – energies below which gas with an intermediate column density of $\sim 10^{23} \text{ cm}^{-2}$ is an effective absorber (cf. Fig. 3).

This above $N_{\text{H}}(\text{scatt})$ column is ≈ 20 times higher than the host galaxy absorbing layer ($N_{\text{H}}(\text{host})$) discussed in the previous section, and would imply correspondingly higher optical reddening. So how viable is this? NGC 7674 is a known luminous infrared galaxy with ongoing star formation and physical interactions with its neighbouring galaxies – all of which could result in obscuring matter being strewn around the host galaxy on multiple scales. Other examples of nearby galaxies with complex multiple layers of absorption identified by *NuSTAR* include NGC 7582 (Rivers et al. 2015) and IC 751 (Ricci et al. 2016). Therefore, the presence of an additional absorber in the innermost parts of the host galaxy that obscures the emergent flux from the nuclear regions is not implausible.

Detailed spatially resolved studies of the nuclear region so far neither require, nor rule out, such a screen. For example, the study of Fischer et al. (2013) does not show an obvious [O III] flux decrement at the nucleus, but the spatial resolution of their spectral sampling is $\approx 30 \text{ pc}$, much larger than the typical sizes of compact tori, and may potentially allow for additional absorbers below the resolution limit. Alternatively, the outflowing gas associated with the powerful nuclear outflow known in NGC 7674 may also serve as a screening medium for X-rays.

In summary, the introduction of $N_{\text{H}}(\text{scatt})$ is clearly somewhat ad hoc and is motivated by the adopted scattering scenario in a fixed Solar metallicity torus model. Nevertheless, we cannot rule it out based upon the present evidence, and we also note that the presence of a PL_{scatt} component, itself, is not surprising, with the measured f_{scatt} value of a few per cent being fully consistent with that seen in other nearby AGN (e.g. Cappi et al. 2006). We have introduced this only as one possible scenario, and as we will discuss in the following section, more complex models could alleviate the need for this screen altogether.

The soft energies can be fitted in a very similar fashion to Model P, with one difference being the presence of a significant, but faint, PL_{soft} component. PL_{soft} dominates only in a very narrow energy range around 2 keV, as a result of which we found that its photon index needed to be fixed, otherwise the fit attempted a very hard slope with contribution to the highest energy *NuSTAR* range. This component is not required in Model P because the reflected component is much more prominent in that case, leaving no deficit around 2 keV (cf. Fig. 2). Since the purpose of this component is to account for the soft energies, we fixed $\Gamma_{\text{soft}} = 2.0$, similar to the spectral slope of the emission from XRBs (e.g. Ranalli, Comastri & Setti 2003). We also checked that allowing small variations of $\Delta \Gamma_{\text{soft}} = \pm 0.3$ do not affect the modelling of the main AGN component.

3.3 Model M: MYTORUS

We first fitted a standard ‘coupled’ MYTORUS model here with all parameters between the los and toroidal scattering components tied to each other. This solution is very similar in essence to Model T, and the fit statistic of $\chi^2/\text{dof} = 325/300$ is compatible with both previous models. Quantitatively, Models T and M differ in that the derived equatorial column density through the torus ($N_{\text{H}}(\text{eq})$) is pegged at the allowed upper model threshold of 10^{25} cm^{-2} in Model M. Similarly, θ_{inc} is just above (and very close to) the allowed lower model threshold of $\theta_{\text{inc}} = 60^\circ$. Such parameter pegging has been seen in other objects also, and reflects the constraint of the assumed doughnut geometry in this model as a result of which the value of $N_{\text{H}}(\text{nuc})$ is directly coupled to θ_{inc} (e.g. Baloković et al. 2014; Gandhi et al. 2014; Lansbury et al. 2015). Smaller inclination angles

are not obscured by the torus in this model, whereas higher θ_{inc} values produce a Compton hump that is too peaky relative to the data. Additional model components are also very similar to Model T. The fitted parameters of this model are listed in Table 2 and the solution is shown in Appendix A, Fig. A1.

3.3.1 Decoupled MYTORUS model

We next tried several versions of the more complex ‘decoupled’ mode in MYTORUS. In this mode, the direct los absorption, the toroidal Compton scattering emission and the fluorescence emission components are not necessarily coupled to each other. By varying the N_{H} , the inclination angles or the relative normalizations associated with these components, one can effectively simulate a variety of scenarios including a clumpy obscurer or varying elemental abundances (for example). This may also potentially allow us to remove the need for the additional ‘ $N_{\text{H}}(\text{scatt})$ ’ layer that was introduced in Section 3.2 for absorbing the scattered PL that dilutes EW(Fe K α).

We first confirmed that simply decoupling the normalization constant of the fluorescence line A_{L} from the normalization of the Compton scattering component A_{S} allowed a very good fit (with a fitted sub-unity value of $A_{\text{L}} = 0.26 \pm 0.06$) with no extra PL_{scatt} component required, equivalent to Model P. The problem is that such a decoupling cannot be self-consistently interpreted as having sub-Solar abundances, because of the assumption of Solar abundances for the Compton scattering component that produces the overall continuum shape of the Compton hump.

We also attempted more complex scenarios, including the possibility of having multiple scatterers. Such a scenario includes two components inclined at orthogonal angles of 0° [face-on] and 90° [edge-on] with $A_{\text{S}} = A_{\text{L}}$ for each component, and is discussed at length by Yaqoob (2012). But these models appeared to require extreme decoupling between the two scatterers. For instance, allowing freely varying cross-normalization constants between these scatterers, the face-on reflection component ($A_{\text{S}0}$ in Yaqoob’s terminology) prefers a normalization $\gtrsim 5$ times stronger than the edge-on component ($A_{\text{S}90}$) responsible for the los obscuration. This implies a strong departure from the default time-steady illuminated MYTORUS geometry with covering factor of 0.5. Such a scenario with strong variability on characteristic time-scales relevant to the inner torus is discussed and argued against in Section 4.2.3.

Alternatively, the column densities between the two scatterers may also be untied. This is equivalent to simulating a clumpy medium with the los obscuration differing from global. Such a solution is shown in Fig. 4. The spectrum can be crudely fit ($\chi^2/\text{dof} = 371/301$) with a low los column associated with the edge-on obscurer $N_{\text{H}}(\text{nuc}) = 1.3 (\pm 0.3) \times 10^{23} \text{ cm}^{-2}$. This component is denoted by ‘MYT(Z90)’ in the figure, as in Yaqoob (2012). However, this also requires a very hard photon index for PL_{AGN} , with $\Gamma = 1.40_{-0.08}^{+0.08}$ pegged at the lower limit allowed by the model. The out-of-sight global column from the face-on scatterer is $N_{\text{H}}(\text{S}0) = 2.4_{-0.8}^{+1.7} \times 10^{24} \text{ cm}^{-2}$ (with corresponding Compton-scattered and fluorescence components denoted by ‘MYT(S0)’ and ‘MYT(L0)’; *Ibid.*). There is more than an order of magnitude difference between the two column densities. In order to prevent the strong normalization departure mentioned in the preceding paragraph, we limited $A_{\text{S}0}$ to a maximum value of 1.20, and the fit does, indeed, want to exceed this limit, with $A_{\text{S}0}$ pegged at $1.20_{-0.07}^{+0.04}$. The scattered fraction is high, with $f_{\text{scatt}} = 0.12_{-0.06}^{+0.04}$ but we stress that there is no additional ad hoc screen associated with the aforementioned $N_{\text{H}}(\text{scatt})$ component in this decoupled model (or in any of the others discussed in this section). The overall fit statistic is much worse ($\Delta \chi^2 = +46$

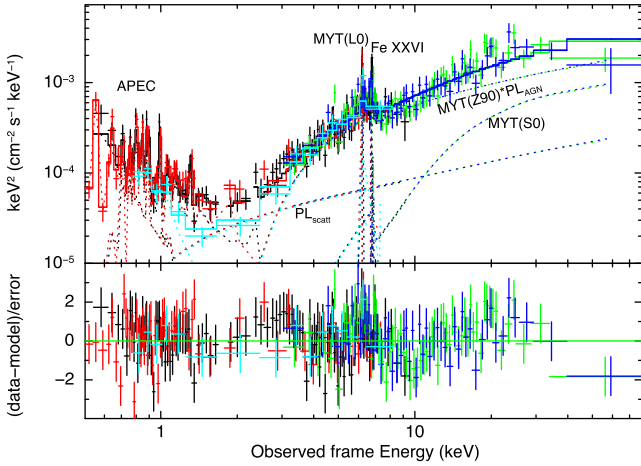


Figure 4. Decoupled MYTORUS model fit with the direct component absorber (MYTZ90) orientation being 90° , and the reflection being dominated by the face-on scatterer MYTSO and its corresponding fluorescence emission from MYTL0.

for a single extra dof) than the default model M solution shown in Table 2.

Scenarios with strong clumpiness have also been discussed for Mrk 3 (Yaqoob et al. 2015; Guainazzi et al. 2016). But such a scenario is not obviously applicable to NGC 7674. Mrk 3 is known to be continuously variable in flux and \log column density, whereas NGC 7674 has been stable since the *BeppoSAX* observations in 1996. Furthermore, it is clear from the discussion of the pegged photon index and normalization values above that the fit is attempting to converge on a harder, more reflection-dominated continuum shape, suggesting that it does prefer a higher \log column density.

Unless the direct PL_{AGN} component can be *robustly* detected, such solutions are highly complex and degenerate, and do not yield any obvious physically useful insights on the nuclear medium beyond our three canonical models discussed in Table 2. This is particularly true for reflection-dominated AGN with no direct detection of PL_{AGN} (e.g. see detailed discussion in Yaqoob 2012 on this point). Therefore, although we cannot rule out more complex models at this stage, we do not investigate the decoupled modes in greater detail herein. Future high signal-to-noise broad-band spectra, and robust detections of reflection features such as the fluorescence Compton shoulder with X-ray calorimeters, could yield more insight on such models.

4 DISCUSSION

4.1 Intrinsic luminosity

Our three models return intrinsic L_{2-10} values ranging over $\approx (3-5) \times 10^{43} \text{ erg s}^{-1}$ for the best-fitting parameters in Table 2. The narrow range of these luminosities is noteworthy, despite the differing geometries inherent to these models. Placing this range in the context of other well-known CTAGN, the luminosity of NGC 7674 is similar to NGC 1068, and is factor of ≈ 2 lower than Mrk 34 (Bauer et al. 2015; Gandhi et al. 2014). The former object is the prototypical reflection-dominated AGN, while the latter is the most luminous known bona fide CTAGN within ~ 250 Mpc. For the *observed* (i.e. absorbed) spectra, we have $F_{2-10}^{\text{obs}} = 7.7 \times 10^{-13} \text{ erg s}^{-1} \text{ cm}^{-2}$, or $L_{2-10}^{\text{obs}} = 1.5 \times 10^{42} \text{ erg s}^{-1}$ – a factor of $\approx 20-30$ times lower than the inferred intrinsic power.

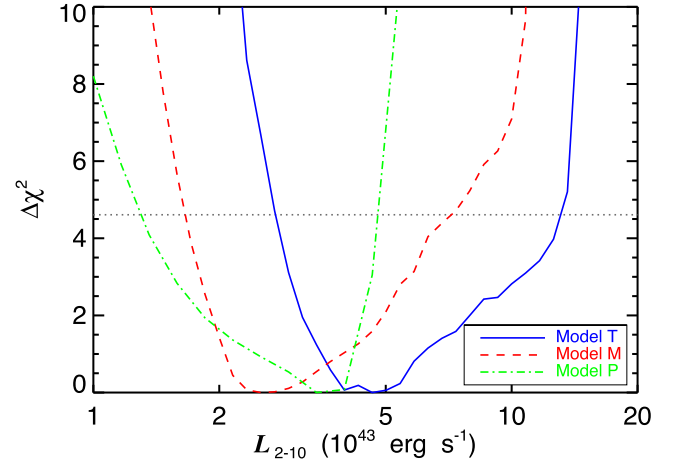


Figure 5. χ^2 contours as a function of L_{2-10} for Models T, M and P. Luminosities are computed over the two-dimensional parameter space of randomized photon index Γ and normalization N values for PL_{AGN} , and the overall one-dimensional *envelope* of corresponding χ^2 values is then plotted. The dotted horizontal line corresponds to $\Delta\chi^2 = 4.61$, or 90 per cent confidence for the two starting parameters Γ and N , relative to the minimum χ^2 for each model.

In order to estimate realistic uncertainties on the intrinsic luminosities, we stepped over a two-dimensional grid of Γ and normalization (N) for the intrinsic PL_{AGN} – the two parameters that determine the absorption-corrected flux (and hence direct luminosity). Carrying out fits over the grid yields a χ^2 value for each combination of Γ and N , and thus effectively for each value of L_{2-10} . Different combinations of the two starting parameters can return identical L_{2-10} values, so the one-dimensional space of χ^2 as a function of L_{2-10} is not unique. But the overall uncertainties can be gauged from the *envelope* of χ^2 contours for all combinations. This envelope is plotted in Fig. 5 for both Models M and T. The figure shows that realistic L_{2-10} uncertainties span the range of $\approx (1.3-13) \times 10^{43} \text{ erg s}^{-1}$, or about an order of magnitude.

Our estimate of the mass of the supermassive black hole in NGC 7674 is $M_{\text{BH}} < 10^{7.43} M_\odot$ (see Appendix A). Using our best-fitting L_{2-10} range of $(3-5) \times 10^{43} \text{ erg s}^{-1}$ together with a bolometric correction likely range of $L_{\text{Bol}}/L_{2-10} \approx 10-20$ (Vasudevan & Fabian 2007), we estimate an Eddington ratio range of $L_{\text{Bol}}/L_{\text{Edd}} > 0.09-0.29$. Including the full range of X-ray luminosity uncertainties expands this range to $L_{\text{Bol}}/L_{\text{Edd}} > 0.04-0.74$, implying the presence of an efficiently accreting AGN.

4.1.1 Multiwavelength comparisons

Multiwavelength scaling relations are very useful for comparison of intrinsic luminosity estimates, especially in the heavily Compton-thick regime where the direct X-ray emission is not detected. Two commonly used multiwavelength indicators of intrinsic AGN power are the mid-infrared continuum and the optical forbidden emission line luminosities, in particular the [O III] $\lambda 5007 \text{ \AA}$ line doublet (e.g. Gandhi et al. 2009; Lamastra et al. 2009, and references therein). We compare NGC 7674 to these relations here.

NGC 7674 has been observed at high angular resolution in the mid-infrared using 8-m class telescopes. It is found to have a $12 \mu\text{m}$ infrared luminosity of $L_{12} = 1.8(\pm 0.3) \times 10^{44} \text{ erg s}^{-1}$ (Asmus et al. 2014). Using this value of L_{12} , the relation between infrared and X-ray luminosities for local AGN (Asmus et al. 2015; Gandhi et al. 2009) predicts an intrinsic L_{2-10} range of $(6-9) \times 10^{43} \text{ erg s}^{-1}$

at 68 per cent confidence, which is marginally higher than the mean best-fitting luminosities from our spectral analysis, but entirely consistent with the full confidence regions for both models shown in Fig. 5. Assuming a 6 μm luminosity lower by a factor of 2 as compared to L_{12} (cf. Goulding et al. 2012) together with the L_6/L_{2-10} relation by Stern (2015) relevant for high-luminosity AGN, the predicted L_{2-10} decreases by a further 0.1 dex. The angular resolution of the mid-infrared observations used (seeing-limited at ≈ 0.4 arcsec) corresponds to a physical scale of ≈ 0.24 kpc for the unresolved nuclear emission at the distance of NGC 7674, and represents the best direct measure of the intrinsic AGN power, with emission from surrounding star formation being largely resolved out. A further check on any contamination by non-AGN components may be obtained from the mid-infrared colour of NGC 7674 as tabulated in the *WISE*/AllWISE catalogue (Wright et al. 2010; Cutri et al. 2013). The $W1 - W2$ colour is 1.16 ± 0.03 mag, which places the source above the colour threshold of $W1 - W2 > 0.8$ identified by Stern et al. (2012), where the mid-infrared emission is likely to be AGN-dominated.

Comparing next to the [O III] emission line, Bassani et al. (1999) present the [O III] $\lambda 5007$ luminosity of the source as $L_{[\text{O III}]}\lambda 5007 = 3.5 (\pm 0.2) \times 10^{42} \text{ erg s}^{-1}$. This value is derived after correcting for dust reddening based upon a Balmer decrement of 4.80. Using the $L_{2-10}/L_{[\text{O III}]}$ relationship presented in Lamastra et al. (2009) with a scatter of 0.6 dex, we expect $L_{2-10} = 5_{-4}^{+7} \times 10^{43} \text{ erg s}^{-1}$ at 68 per cent confidence, overlapping well with our spectrally modelled intrinsic luminosity range.

In summary, the best-fitting X-ray luminosity measured from our spectral analysis agrees well with the multiwavelength comparisons above, especially when considering the full range of realistic uncertainties on the spectral modelling (Fig. 5). This is encouraging given that this source appears to be heavily Compton-thick and that the true torus geometry is unknown. Broad-band spectral modelling of high signal-to-noise X-ray data is what enables us to get such good agreement.

4.1.2 The soft X-ray component

The absorption-corrected luminosity in the XIS 0.5–2 keV band is $L_{0.5-2}^{\text{APEC}} \approx 4.5 \times 10^{42} \text{ erg s}^{-1}$. This is for both APEC components combined, but is dominated by a factor of 4 by the lower temperature component. Using the relation for star-forming galaxies by Mineo, Gilfanov & Sunyaev (2012) between the thermal component luminosity and the star formation rate (SFR), we estimate an X-ray-derived $\text{SFR}_{\text{X-ray}} \approx 9 \times 10^3 M_{\odot} \text{ yr}^{-1}$.

This may be compared to the infrared-derived SFR, based upon the far-infrared continuum luminosity L_{IR} and its relation to SFR_{IR} (Kennicutt 1998). For NGC 7674, $L_{\text{IR}} \approx 10^{11.56} L_{\odot}$ (Koss et al. 2013), which yields $\text{SFR}_{\text{IR}} \approx 60 M_{\odot} \text{ yr}^{-1}$. This is more than two orders of magnitude lower than the estimated $\text{SFR}_{\text{X-ray}}$, and implies that starburst-powered APEC components alone are an unphysical representation of the soft X-ray emission in NGC 7674. Photoionization could instead power some of this, as we have already alluded to on several occasions. We also note that uncertainties related to absorption correction of soft X-rays cannot account for the extremely high $\text{SFR}_{\text{X-ray}}$. Ignoring absorption corrections and using the observed (i.e. absorbed) $L_{0.5-2}^{\text{APEC}}$ directly still results in $\text{SFR}_{\text{X-ray}} \approx 950 M_{\odot} \text{ yr}^{-1}$, far higher than SFR_{IR} .

We note, however, that the estimated value of SFR_{IR} is itself large. For example, it is about 10 times above the SFR of the prototypical starburst galaxy M82 (e.g. Telesco & Harper 1980). Such high star

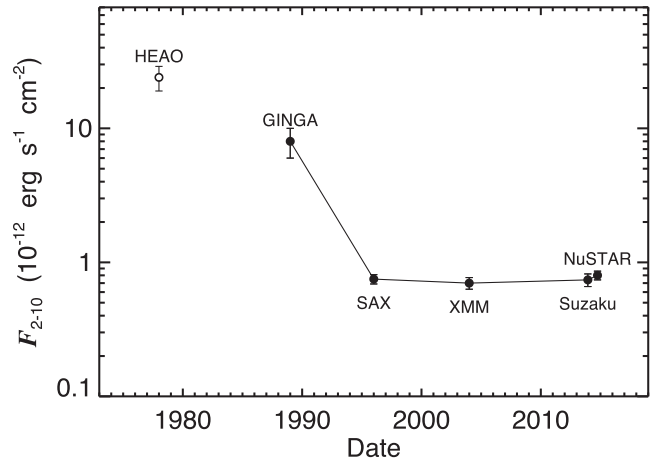


Figure 6. Long-term 2–10 keV observed flux light curve of NGC 7674 spanning $\sim 1977/78$ (the *HEAO* epoch) to late 2014 (*NuSTAR*). The *HEAO* measurement is segregated from the other fluxes to stress its potentially uncertain nature.

formation is likely to power extended ionized gas emission, and we will return to possible implications of this in Section 4.3.3.

4.2 The nature of the long-term flux changes

Fig. 6 shows the long-term X-ray light curve of NGC 7674 over a period of about 37 yr. As first noted by Bianchi et al. (2005), the source showed a decline by a factor of ~ 3 in the 2–10 keV band between the first detection by *HEAO* in the late 1970s and the *Ginga* measurement in 1989, followed by a further order of magnitude flux decrease in 1996 when *BeppoSAX* identified the source as a CTAGN (Malaguti et al. 1998). Thereafter, the source flux has remained constant with no significant spectral or flux variation for the past ≈ 20 yr. This now includes the most recent *Suzaku* and *NuSTAR* observations. The individual *Swift* observations spanning the period of 2011–2014 detailed in Appendix A also show fluxes or detection limits broadly consistent with *BeppoSAX*, *Suzaku* and *NuSTAR*. Finally, the custom analysis of the *Swift*/BAT maps by Koss et al. (2013) shows a weak detection with flux $F_{14-195} = 9.9_{-2.4}^{+5.1} \times 10^{-12} \text{ erg s}^{-1} \text{ cm}^{-2}$ consistent with *NuSTAR*. For instance, our Model T, when extrapolated to the energy range of 14–195 keV, implies best-fitting fluxes ranging over $(8.4\text{--}9.3) \times 10^{-12} \text{ erg s}^{-1} \text{ cm}^{-2}$ between the mission cross-calibration uncertainties.

Here, we examine the viability of the inferred long-term decline and its implications.

4.2.1 On the possibility of contamination by another source

Could the pre-*BeppoSAX* flux decline be associated with a contaminating source, unrelated to the AGN? The observed luminosities at the *HEAO* and *Ginga* epochs are above $10^{42} \text{ erg s}^{-1}$ – already too high to be easily associated with XRBs within the host galaxy. An XRB within our Galaxy that just happens to lie along the same los as NGC 7674 cannot be ruled out, though the high Galactic latitude ($b = -48^\circ$) makes this unlikely.

Regarding contamination by other AGN, there is only one possible bright source in the recent 70 month all sky *Swift*/BAT hard X-ray survey, which could potentially have contaminated both the *HEAO* and *Ginga* fields of view. This is PKS 2325+093 that lies at a separation of 0.9° from NGC 7674 and shows a BAT flux of F_{14-195}

$\approx 3 \times 10^{-11} \text{ erg s}^{-1} \text{ cm}^{-2}$ (Baumgartner et al. 2013). However, this source lies outside the *HEAO* positional error box of NGC 7674 (Bianchi et al. 2005). Moreover, PKS 2325+093 shows a very hard spectrum, at least in the BAT band, with $\Gamma_{\text{BAT}} = 1.29 \pm 0.28$. This is much harder than the spectral shape inferred for the *Ginga* observation below $\approx 10 \text{ keV}$ by Bianchi et al. (2005). Although a drastic change in spectral curvature around 10 keV cannot be ruled out, the combined weight of evidence appears to disfavour contamination.

4.2.2 Background uncertainties

Measurements with non-imaging detectors such as the *HEAO* A-1 Large Area Sky Survey instrument (Wood et al. 1984) and the *Ginga* Large Area Counter (Turner et al. 1989) are prone to uncertain background estimates, especially at low source flux levels. However, as discussed by Bianchi et al. (2005), the background for the observation of NGC 7674 is based on a scanning observation obtained close in time to the target (Awaki et al. 1991). These background scans result in noise estimates that are more reliable than model estimates typically adopted for non-imaging detectors.

Therefore, the *Ginga* flux, at least, is considered to be reliable and is significantly higher than that seen by subsequent missions, by about a factor of 10. The *HEAO* flux, on the other hand, may well be affected by the above uncertainties, and we do not consider it as a strong constraint in the following discussion.

4.2.3 The ‘switched-off’ AGN scenario

Assuming that the luminosity change (at least that between *Ginga* and subsequent missions) is associated with the AGN in NGC 7674 itself, there are then two possible implications: the AGN could either have faded dramatically (an effective ‘switch-off’, as is referred to hereafter), or it could have become enshrouded within Compton-thick material after the *Ginga* observation. We consider these cases here.

The switched-off AGN scenario was examined by Bianchi et al. (2005), motivated by the fact that, unlike other changing-look AGN in which N_{H} variations occur relatively frequently, NGC 7674 did not show any flux or spectral variations in post-*BeppoSAX* observations. In this scenario, the observed reflection component dominating at hard X-rays is expected to be delayed with respect to the incident PL_{AGN} that has now faded. Similarly, the absorbed scattered component (PL_{scatt}) included in our Models T and M (cf. Fig. 3) would also be interpreted as a delayed component scattered in to the los from material on $\sim \text{pc}$ scales, or larger. The current PL_{AGN} flux level cannot be higher than that this PL_{scatt} component, which has a deabsorbed luminosity $L_{2-10}^{\text{scatt}} \approx 2 \times 10^{42} \text{ erg s}^{-1}$ – an order of magnitude fainter than inferred during the *Ginga* observation epoch (1989). In Model P, where no scattering component is required (cf. Fig. 2), the constraint on the current intrinsic AGN luminosity is even more stringent, with L_{2-10} expected to be 10 times lower still.

Assuming that the source switched off between the *Ginga* (1989) and *BeppoSAX* (1996) epochs around 1993, i.e. $21 \pm 3 \text{ yr}$ before the *NuSTAR* observation, the absence of any flux change since then places a minimum limit on the radius (R) of an axisymmetric reflector $R = 3.2 \text{ pc}$ based upon a simple consideration of the light travel time from the far wall of a nearly edge-on reflector. Considering the average travel time over the full body of the reflector, and/or intermediate inclinations angles, would push up the lower limit on R . While extended reflectors on scales of up to $\sim 150 \text{ pc}$ have been observed in several CTAGN (e.g. NGC 4945: Marinucci et al. 2012;

Circinus, Arévalo et al. 2014; NGC 1068: Bauer et al. 2015), the studies so far find that these extended components make relatively minor flux contributions compared to the compact reflectors.

In fact, detailed studies of type 1 AGN have shown that the bulk of the neutral Fe $K\alpha$ emission line arises at very compact scales of the dust sublimation radius (R_{sub}) or smaller (see detailed discussion in Gandhi, Hönig & Kishimoto 2015, and references therein), and in the orientation-based unification scheme, this would also hold for obscured and CTAGN viewed at higher inclination angles. For NGC 7674, R_{sub} is estimated to be $\approx 0.1_{-0.04}^{+0.05} \text{ pc}$ based upon infrared luminosity scaling relations determined at high angular resolution where the AGN can be effectively isolated from surrounding star formation (Hönig et al. 2010). This size scale is about 30 times smaller than the lower limit on R above.

In other words, in the switched-off AGN scenario, a typical (sub)-pc scale torus reflector would be expected to respond to a decline of the intrinsic continuum on time-scales faster than seen in Fig. 6, and we would have expected to see some change in the reflected component fluxes under the switched-off AGN scenario by now.

4.2.4 Clumpy Compton-thick obscurer scenario

In the obscured AGN scenario, the source became obscured sometime between the *Ginga* (1989) and the *BeppoSAX* (1996) epochs, and is now fully covered by CT material along the los. Varying nuclear obscuration is common in AGN, but extreme transitions between Compton-thick and Compton-thin states are not (Markowitz, Krumpe & Nikutta 2014). So it is interesting to examine whether the obscurer in NGC 7674 may somehow be atypical. Some qualitative constraints on the nature and geometry of the obscuring clouds are possible as follows.

First, we argue that the global covering factor of the material is unlikely to be atypically low. This is because the reflection component we observe is strong. The observed reflected luminosity (L_{obs}) scales approximately with intrinsic luminosity (L_{int}) as

$$L_{\text{obs}} \sim L_{\text{int}} \Omega a, \quad (1)$$

where Ω is the solid angle of the reflector and a is the albedo. The physical models that we have used in our spectral fits assume fairly typical geometrical covering factors for the torus, and yield estimates of L_{int} that are in reasonable agreement (to within a factor of a few) with other multiwavelength indicators (Section 4.1.1). If the reflector had a small covering factor Ω , the corresponding geometrical correction would imply much higher values of L_{int} .

The complete lack of recent X-ray flux variability also supports this. Whereas an extended distribution of clouds can naturally spread out and dampen variations in the reflected flux relative to any variability in the direct AGN radiation, this is not possible in the low covering factor limit. Indeed, most reflection-dominated CTAGN are observed to show little, or no flux variations at all [cf. two well-studied examples include Circinus (Arévalo et al. 2014) and NGC 5643 (Annuar et al. 2015), although sensitive observations have recently caught a transient column density change in NGC 1068 (Marinucci et al. 2016)]. Sources where significant flux variability is observed (e.g. NGC 4945 (Puccetti et al. 2014), ESO 565-G019 (Gandhi et al. 2013) and IC 751 (Ricci et al. 2016) tend to be *mildly* CTAGN or significantly clumpy, with the direct transmitted component being stronger than the reflection component over at least some portion of the hard X-ray regime. In particular, many observations support the presence of a small Ω for the obscurer in NGC 4945 (e.g. Madejski et al. 2000, though there are other possible scenarios as discussed by Brightman et al. 2015).

The emerging scenario for NGC 7674 then is that a patchy distribution of clouds obscures the nucleus with a covering factor fairly typical of standard torus models. By the time of the *BeppoSAX* observation in 1996, a cloud ensemble with CT column density had fully obscured the los to the nucleus, and this ensemble has continuously covered the los ever since.

Unlike changing-look AGN, however, NGC 7674 does not show frequent flux or spectral variability. This raises a complementary point of view that the past high state caught by *Ginga* was instead a transient near-complete *unveiling* of the nucleus caused by the los passing through a hole in the patchy obscurer. Assuming relatively sharp optical depth edges to the obscuring clouds, the time gap of ≈ 7 yr between the *Ginga* and *BeppoSAX* observations is probably a strong upper limit to the time taken to cover the AGN X-ray emission region, which is expected to be highly compact (e.g. Risaliti et al. 2007). In other words, the ‘unveiling’ could have been very brief, and *Ginga* may have simply been fortunate to catch the event.

Interestingly, converting the observed 1989 *Ginga* flux of $8(\pm 2) \times 10^{-12}$ erg s $^{-1}$ cm $^{-2}$ (Bianchi et al. 2005) to a luminosity yields $L_{2-10} \approx 2 \times 10^{43}$ erg s $^{-1}$, again consistent with our spectral analysis results based upon the more recent data (Section 4.1). The effect of absorption in the *Ginga* spectrum appears minimal. This consistency provides additional support for the obscured AGN scenario.

Finally, we note that given the uncertainty associated with the *HEAO* flux measurement, there is no strong constraint on the pre-*Ginga* flux evolution. If the *HEAO* flux measurement were to be correct, the above analysis would imply that the AGN would have been *intrinsically* more luminous by a factor of ≈ 3 during the *HEAO* era. In this case, explaining the long-term flux evolution would require a combination of source fading (between *HEAO* and *Ginga*) followed by patchy obscuration, which seems unlikely.

4.3 On the weakness of the Fe K α line

In our analysis, we found that the source has a relatively weak neutral Fe K α emission line, and showed that this can be reproduced by assuming either a low elemental abundance (Model P), or an absorbed scattering solution (Models T and M). Here, we first place this result in context of other local CTAGN (Section 4.3.1) and then briefly investigate one other potential scenario of iron line dilution by a jet (Section 4.3.2). In Section 4.3.3, we extend the comparison with other objects to higher redshifts (especially those that show prominent *ionized* Fe lines), before finally examining the broader implications of Fe line measurements in deep AGN surveys in Section 4.4.

4.3.1 Comparison with other bona fide CTAGN

CTAGN are usually associated with strong Fe K α emission lines with EW of $\gtrsim 1$ keV. Our work shows a much weaker EW ≈ 0.4 keV (also reported by Bianchi et al. 2005), but our spectral modelling of NGC 7674 also consistently finds high Compton-thick column densities using several different spectral models.

In fact, comparing to other reflection-dominated AGN (such as NGC 1068, NGC 5643, Mrk 34 and others with $N_{\text{H}} \gtrsim 10^{25}$ cm $^{-2}$) amongst the local *bona fide* CTAGN population (Della Ceca et al. 2008; Goulding et al. 2012; Gandhi et al. 2014), NGC 7674 appears to have one of the weakest neutral Fe fluorescence lines. This is demonstrated in Fig. 7, where NGC 7674 stands out in the distribution of EW distribution of bona fide CTAGN compiled by Gandhi et al. (2014). The EW values are taken from relevant

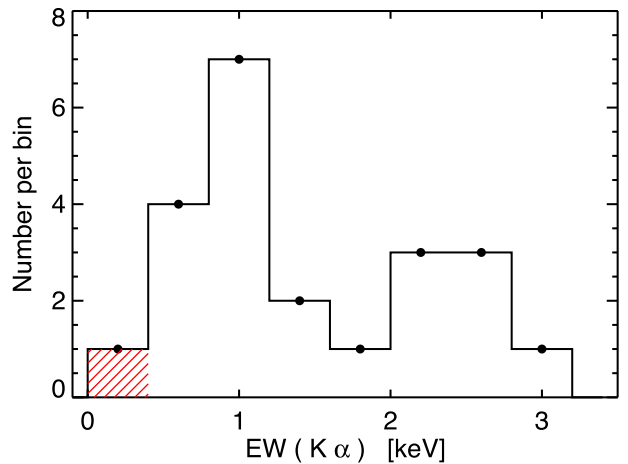


Figure 7. Distribution of EWs of the neutral Fe K α emission line for the bona fide CTAGN compiled in Gandhi et al. (2014). The red hatched region corresponds to NGC 7674 (EW = $0.38_{-0.09}^{+0.10}$ keV).

recent references in the same paper, or (where recent values are not published) from the compilation of Della Ceca et al. (2008). They are mostly based upon PL fits to the continuum together with Gaussian line components. Three sources have been excluded because of published works questioning their bona fide CTAGN nature, or showing that they have highly complex geometries: Mrk 3 (EW $\approx 1.0 \pm 0.3$ keV; Yaqoob et al. 2015; Guainazzi et al. 2016), NGC 7582 (EW $\approx 0.6_{-0.1}^{+0.6}$ keV; Rivers et al. 2015) and NGC 4939 (EW $\approx 0.5_{-0.2}^{+0.4}$ keV; Maiolino et al. 1998). Their exclusion does not affect the relative position of NGC 7674.

4.3.2 Dilution by a jet?

One other possibility may be that a jet is diluting the continuum underlying the Fe K α emission line and hence effectively weakening the observed EW. Such dilution has been inferred in several broad-line radio galaxies (e.g. Eracleous, Sambruna & Mushotzky 2000), and also in broad absorption line quasars (e.g. Luo et al. 2013).

In the case of NGC 7674, however, we consider this possibility to be unlikely for several reasons. Although NGC 7674 is a known radio source, it is classified as radio-quiet (Xu et al. 1999). Then there is the distinct lack of X-ray variability at 2–10 keV as probed by several missions over the past ~ 20 yr. Non-thermal emission from a jet is expected to be significantly variable, especially when probed on multiple (long) time-scales that we are now able to sample (Fig. 6).

Finally, one may try to quantify the expected flux from a jet irrespective of the above considerations. The core of NGC 7674 has a morphology extended over ≈ 1 kpc, characteristic of radio galaxies (e.g. Momjian et al. 2003). There is evidence of complex interactions of the radio ejecta with the interstellar medium – complex enough that the location of the AGN itself is unclear in the radio (Momjian et al. 2003). The reported integrated 5 GHz nuclear radio flux density is 67 mJy (Condon, Frayer & Broderick 1991), corresponding to a monochromatic luminosity density of $L_{5\text{GHz}} = 1.3 \times 10^{30}$ erg s $^{-1}$ Hz $^{-1}$.

The above luminosity is lower than the power typically associated with radio-loudquasars (RLQs) as well as radio-intermediate quasars (RIQs). For example, Miller et al. (2011) studied samples of RIQs and RLQs and showed that there exists an ‘X-ray excess’

above that seen in radio-quiet sources. The excess scales with radio luminosity and could be associated with a jet contribution to X-rays. At the observed luminosity density of NGC 7674, the correlation between the X-ray excess and radio luminosity found by Miller et al. (2011) is consistent with no jet-related X-ray excess. Their correlation needs to be extended below their lower luminosity limit and would instead predict an X-ray deficit of -0.14 ± 0.09 in their adopted units of $\ell_x - \ell_{x, \text{RQQ}}$.

Instead of using the correlation for quasars, one may instead try using the correlation between radio power and the jet-related unabsorbed X-ray PL luminosities for lower luminosity 3CRR sources presented by Hardcastle, Evans & Croston (2009). In the terminology used by Hardcastle et al., the X-ray PL luminosity is $L_{X, u}$, with the X-ray band being $\approx 0.4\text{--}8$ keV, and a fixed spectral slope $\Gamma_{\text{jet}} = 2$. From the reported 5 GHz radio flux density, we predict $L_{X, u} \approx 10^{41}$ erg s $^{-1}$, or $F_{2-10} = 3 \times 10^{-14}$ erg s $^{-1}$ cm $^{-2}$. This is more than a factor of 20 fainter than our observed F_{2-10} . Accounting for a scatter of 0.56 dex in the relation of Hardcastle et al. (2009), the predicted jet X-ray flux is still lower than the observed flux by a factor of 6, rendering this scenario unlikely.

4.3.3 On the strength of ionized Fe and the relation to other powerful infrared galaxies

A variety of studies have found that distant sources with high bolometric power, including ultraluminous infrared galaxies (ULIRGs) and sub-mm galaxies, show preferentially strong ionized Fe lines such as Fe XXV (6.7 keV) and Fe XXVI (6.97 keV; e.g. Iwasawa et al. 2009; Lindner et al. 2012; Gilli et al. 2014). The neutral Fe K α (6.4 keV) line is extremely weak or undetected in many of these systems. This may be attributable either to the neutral reflection component being heavily embedded within the torus as seen by us, or to a highly ionized interstellar medium that is being energized by starburst activity, or a combination of the two effects. Iwasawa et al. (2012) further suggest that preferentially strong ionized emission lines may be connected to high accretion rates on the central AGN.

With a bolometric infrared power of $10^{11.56} L_{\odot}$ (Koss et al. 2013), NGC 7674 lies in the regime of luminous infrared galaxies. This is lower than, but approaching, the regime associated with ULIRG luminosities. Such an intermediate luminosity could explain why the source displays *both* a neutral and an ionized Fe line with strengths comparable to within a factor of about 2. Our estimate of the Eddington ratio of the AGN in Section 4.1 is as high as ≈ 0.4 , and this could be even higher if M_{BH} has been overestimated (see Appendix A). Brightman et al. (2016) also compile evidence showing that some CTAGN (with steep X-ray PL photon indices) may exhibit high Eddington fractions. If so, NGC 7674 would be a local analogue of the more bolometrically luminous systems with high accretion rates studied by Iwasawa et al. (2012). A more robust M_{BH} estimate will be needed to test these parallels.

Finally, we note that a strong ionized Fe XXVI emission feature may be accompanied by an ionized underlying continuum. So it is possible that the scattered component introduced in Section 3.2 actually arises from photoionized or hot collisionally ionized gas that also self-consistently produces Fe XXVI and some of the soft emission. The possible need for a photoionized component was discussed in Section 4.1.2. We attempted to fit the data as such, by replacing the absorbed PL $_{\text{scatt}}$ component from our base Model T with a photoionized model based upon the publicly available CLOUDY code (Ferland et al. 1998). Examples of such fits can be found for various other AGN, including Mrk 573 (Bianchi et al. 2010) and

ESO 138-G001 (De Cicco et al. 2015). Reasonable fits were possible without PL $_{\text{scatt}}$, but we found that the photoionized component was required to be extremely strong relative to the Compton-thick torus, and that it dominated over the entire energy range to up ~ 10 keV. Although we cannot rule out such a model, photoionized components are usually much fainter (Bianchi et al. 2005; De Cicco et al. 2015). High-spectral resolution observations will be required to test this scenario in further detail.

4.4 Implications for identifying CTAGN at a low X-ray signal to noise

The fact that NGC 7674 shows a weak Fe K α emission line, yet clearly prefers a Compton-thick los column, has potentially important implications for the study of more distant AGN in deep surveys where the signal to noise is typically much weaker than in our data. Using simulations, Koss et al. (2015) found that robust characterization of typical nearby CTAGN, such as NGC 3393, is only possible at relatively low redshifts of $z \lesssim 0.2$ if one relies upon detection of the Fe K α emission line and broad-band continuum for spectral modelling.

Our results on NGC 7674 further complicate this issue. With a value of EW(Fe K α) weaker by a factor of ≈ 3 than in NGC 3393, it becomes even more difficult to identify an object as being Compton-thick. We demonstrate this by carrying out a simulation of a source with a model spectrum identical to NGC 7674, but with a lower flux of $F_{8-24} = 5 \times 10^{-13}$ erg s $^{-1}$ cm $^{-2}$. Although four times fainter than NGC 7674 in the same band, this flux level lies more than an order of magnitude above the deepest flux level being probed in ongoing deep and wide *NuSTAR* surveys (Aird et al. 2015; Civano et al. 2015; Harrison et al. 2016; Mullaney et al. 2015). We simulated *NuSTAR* spectra for both FPMs using the default background and response simulation files⁶ provided by the *NuSTAR* team, and assuming an exposure time of 100 ks. We also introduced a small redshift $z = 0.25$, effectively assuming an intrinsic X-ray luminosity $L_{2-10} \approx 10^{45}$ erg s $^{-1}$, characteristic of luminous AGN likely to be found in deep surveys.

The simulated spectra are shown in Fig. 8. The rising continuum slope (from the Compton hump of our baseline Model T) is clearly visible. We first fitted the simulated data with a simple PL model (not shown), which yielded $\Gamma = 1.1 \pm 0.2$ with $\chi^2/\text{dof} = 27/29$. No additional Fe K α emission line is required for the fit. This hard slope is suggestive of the need for obscuration. However, including redshifted photoelectric absorption and reflection with a TORUS model implies an N_{H} of only $2.2^{+0.9}_{-0.8} \times 10^{23}$ cm $^{-2}$ for a fixed canonical $\Gamma = 1.8$, i.e. a Compton-thin solution (the solution shown in the figure). This is a direct result of the lack of a strong Fe K α emission line.

The newer torus models are now being widely used by the community for self-consistent modelling of the nuclear obscuring material, and these have proven to be very successful at characterizing objects well into the Compton-thick regime. However, most of the publicly available torus models do not allow varying elemental abundances which, as we discuss in Section 3.2, means that sources like NGC 7674 cannot be fit without additional complexity. In any case, such model complexity is often not viable for fitting low signal-to-noise data, with the result that the column density, and hence intrinsic luminosity, of distant AGN may be underestimated.

A full assessment of the resultant bias in deep surveys is beyond the scope of this paper, until the frequency of weak Fe K α CTAGN

⁶ <http://sc.nustar.caltech.edu>

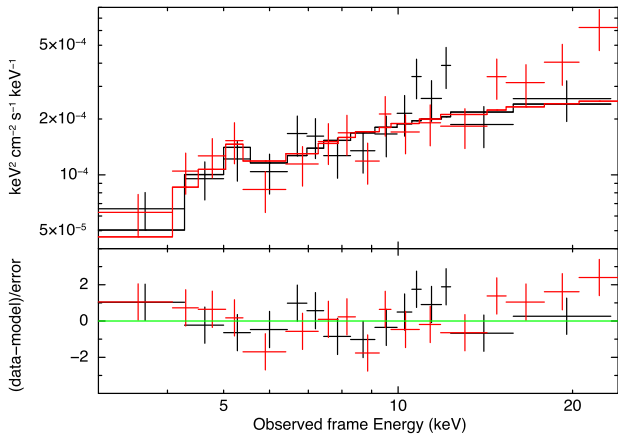


Figure 8. *NuSTAR* simulated spectra for two FPMs assuming our Model T best-fitting model to NGC 7674, but with a flux lower by a factor of 4 and shifted to $z = 0.25$. The simulation is for 100 ks of exposure time per FPM. The histograms show best-fitting TORUS model to the faked data, and are fitted with $N_{\text{H}} = 2.2^{+0.9}_{-0.8} \times 10^{23} \text{ cm}^{-2}$ and $\Gamma = 1.8$ for canonical fixed values of $\theta_{\text{tor}} = 60^\circ$ and $\theta_{\text{inc}} = 87^\circ$, i.e. a Compton-thin solution. The fit statistic is $\chi^2/\text{dof} = 34/29$.

such as NGC 7674 can be established. Independent selection of large samples of CTAGN candidates based upon X-ray spectral diagnostics and on multiwavelength indicators (i.e. high ratios of L_{MIR} or $L_{[\text{O III}]}$ to observed L_{2-10}) could be an informative first step in this direction (cf. Rovilos et al. 2014). Similarly, we recommend the use of varying elemental abundances as an additional free parameter in model fitting when signal to noise allows.

If we are to make robust progress on the Compton-thick selection problem, multiple redundant cross-checking methods must be employed (the work of Brandt & Alexander 2015 contains a recent, comprehensive analysis of various techniques in the literature).

5 SUMMARY

We have presented *NuSTAR* spectroscopy of the local reflection-dominated AGN NGC 7674. Together with unpublished *Suzaku* and *Swift* data, we carried out broad-band X-ray modelling of the 0.5–78 keV spectrum assuming three geometries of the nuclear obscurer/reflector. The best-fitting model in all cases requires a nuclear column density of obscuring gas $N_{\text{H}}(\text{nuc})$ of at least $3 \times 10^{24} \text{ cm}^{-2}$ and possibly much higher, with an absorption-corrected luminosity $L_{2-10} = (3-5) \times 10^{43} \text{ erg s}^{-1}$ (Table 2), agreeing with mid-infrared continuum and forbidden optical [O III] emission line indicators. The full uncertainty range on L_{2-10} spans $\approx (1-13) \times 10^{43} \text{ erg s}^{-1}$ (Fig. 5). A relatively weak neutral Fe $K\alpha$ emission line (EW ≈ 0.4 keV) at 6.4 keV is seen, together with a comparatively strong ionized Fe line consistent with 6.97 keV emitted by Fe XXVI. We explore a variety of scenarios to explain the line complex and suggest that NGC 7674 may be similar to more powerful ULIRGs that also show similar trends of line complexity, possibly related to a high accretion rate (Section 4.3.3).

We have presented an X-ray light curve spanning 37 yr (Fig. 6), and find that the observed source X-ray flux has remained constant for about 20 yr, prior to which it was brighter by a factor of at least ≈ 10 when observed by *Ginga*. A past *HEAO* detection was three times brighter still, but background uncertainties make this measurement less reliable. A faded/switched-off AGN scenario requires a reflector size of at least 3 pc, which is ≈ 30 times larger than the dust sublimation radius of the canonical pc-scale torus in

NGC 7674, and thus is not a preferred explanation for the observed fading (Section 4.2.3).

The alternative scenario is that a clumpy Compton-thick obscuring medium has been continuously obscuring the source for $\approx 21 \pm 3$ yr since the mid-1990s. Unlike known changing-look AGN, however, NGC 7674 does not show frequent flux or spectral shape transitions, with none observed since the *BeppoSAX* observation. If a steady-state patchy obscurer does surround the nucleus, the past high state of NGC 7674 could have represented a temporary unveiling of the nucleus (Section 4.2.4). It is also noteworthy that the source has been an optical Seyfert 2 for more than 30 yr, implying that the source has shown no evidence of being a ‘changing-look’ AGN over significant periods of time in the optical. The relation between the strong nuclear outflow and the X-ray-obscuring medium, and whether the outflow is connected to the past fading, also remains to be investigated. Continued monitoring of the source will be important, as will high-spatial and spectral resolution multi-wavelength observations to understand these connections.

The weakness of the neutral Fe $K\alpha$ emission line implies that canonical torus covering factors and Solar metallicities cannot be used in order to derive absorption correction factors. This is relevant for surveys of distant, fainter AGN where the signal to noise of the data do not allow detailed fitting of individual sources and simplifying assumptions are introduced for spectral modelling (Section 4.4).

ACKNOWLEDGEMENTS

This research has made use of data from the *NuSTAR* mission, a project led by the California Institute of Technology, managed by the Jet Propulsion Laboratory, and funded by the National Aeronautics and Space Administration. We thank the *NuSTAR* Operations, Software and Calibration teams for support with the execution and analysis of these observations. This research has made use of the *NuSTAR* Data Analysis Software (NUSTARDAS) jointly developed by the ASI Science Data Center (ASDC, Italy) and the California Institute of Technology (USA). This work made use of data supplied by the UK Swift Science Data Centre at the University of Leicester (Evans et al. 2009). PG thanks the Science and Technology Facilities Council (STFC) for support (grant reference ST/J003697/2). AC and AM acknowledge support from the ASI/INAF grant I/037/12/0-011/13. AC acknowledges the Caltech Kingsley visitor programme. We acknowledge financial support from Majlis Amanah Rakyat (MARA) Malaysia (AA), STFC grants ST/I0015731/1 (DMA) and ST/K501979/1 (GBL). WNB acknowledges California Institute of Technology (Caltech) *NuSTAR* subcontract 44A-1092750. SB acknowledges financial contribution from the agreement ASI/INAF I/037/12/0. We also acknowledge NASA NuSTAR A01 Award NNX15AV27G (FEB), CONICYT-Chile grants Basal-CATA PFB-06/2007 (FEB, CR), FONDECYT Regular 1141218 (FEB, CR), ‘EMBIGGEN’ Anillo ACT1101 (FEB, CR) and the Ministry of Economy, Development, and Tourism’s Millennium Science Initiative through grant IC120009, awarded to The Millennium Institute of Astrophysics, MAS (FEB). We thank the referee for detailed comments that helped us to make the presentation of results clearer and to place the discussion on a more robust footing.

REFERENCES

- Aird J. et al., 2015, *ApJ*, 815, 66
 Annuar A. et al., 2015, *ApJ*, 815, 36

- Arévalo P. et al., 2014, *ApJ*, 791, 81
- Arnaud K. A., 1996, in Jacoby G. H., Barnes J., eds, *ASP Conf. Ser. Vol. 101, Astronomical Data Analysis Software and Systems V*. Astron. Soc. Pac., San Francisco, p. 17
- Asmus D., Hönic S. F., Gandhi P., Smette A., Duschl W. J., 2014, *MNRAS*, 439, 1648
- Asmus D., Gandhi P., Hönic S. F., Smette A., Duschl W. J., 2015, *MNRAS*, 454, 766
- Awaki H., Koyama K., Inoue H., Halpern J. P., 1991, *PASJ*, 43, 195
- Ballantyne D. R., Draper A. R., Madsen K. K., Rigby J. R., Treister E., 2011, *ApJ*, 736, 56
- Baloković M. et al., 2014, *ApJ*, 794, 111
- Barthelmy S. D. et al., 2005, *Space Sci. Rev.*, 120, 143
- Bassani L., Dadina M., Maiolino R., Salvati M., Risaliti G., della Ceca R., Matt G., Zamorani G., 1999, *ApJS*, 121, 473
- Bauer F. E. et al., 2015, *ApJ*, 812, 116
- Baumgartner W. H., Tueller J., Markwardt C. B., Skinner G. K., Barthelmy S., Mushotzky R. F., Evans P. A., Gehrels N., 2013, *ApJS*, 207, 19
- Bian W., Gu Q., 2007, *ApJ*, 657, 159
- Bianchi S., Guainazzi M., Matt G., Chiaberge M., Iwasawa K., Fiore F., Maiolino R., 2005, *A&A*, 442, 185
- Bianchi S., Chiaberge M., Evans D. A., Guainazzi M., Baldi R. D., Matt G., Piconcelli E., 2010, *MNRAS*, 405, 553
- Blackburn J. K., 1995, in Shaw R. A., Payne H. E., Hayes J. J. E., eds, *ASP Conf. Ser. Vol. 77, Astronomical Data Analysis Software and Systems IV*. Astron. Soc. Pac., San Francisco, p. 367
- Bohlin R. C., Savage B. D., Drake J. F., 1978, *ApJ*, 224, 132
- Brandt W. N., Alexander D. M., 2015, *A&AR*, 23, 1
- Brightman M., Nandra K., 2011, *MNRAS*, 413, 1206
- Brightman M. et al., 2015, *ApJ*, 805, 41
- Brightman M. et al., 2016, *ApJ*, 826, 93
- Burrows D. N. et al., 2005, *Space Sci. Rev.*, 120, 165
- Cappellari M., Emsellem E., 2004, *PASP*, 116, 138
- Cappi M. et al., 2006, *A&A*, 446, 459
- Civano F. et al., 2015, *ApJ*, 808, 185
- Comastri A., Setti G., Zamorani G., Hasinger G., 1995, *A&A*, 296, 1
- Condon J. J., Frayer D. T., Broderick J. J., 1991, *AJ*, 101, 362
- Cutri R. M. et al., 2013, *Explanatory Supplement to the AllWISE Data Release Products*, Technical report
- De Cicco M., Marinucci A., Bianchi S., Piconcelli E., Violino G., Vignali C., Nicastro F., 2015, *MNRAS*, 453, 2155
- Della Ceca R., Severgnini P., Caccianiga A., Comastri A., Gilli R., Fiore F., Piconcelli E., Malaguti P., Vignali C., 2008, *Mem. Soc. Astron. Ital.*, 79, 65
- Dickey J. M., Lockman F. J., 1990, *ARA&A*, 28, 215
- Eracleous M., Sambruna R., Mushotzky R. F., 2000, *ApJ*, 537, 654
- Evans P. A. et al., 2009, *MNRAS*, 397, 1177
- Feldman F. R., Weedman D. W., Balzano V. A., Ramsey L. W., 1982, *ApJ*, 256, 427
- Ferland G. J., Korista K. T., Verner D. A., Ferguson J. W., Kingdon J. B., Verner E. M., 1998, *PASP*, 110, 761
- Fischer T. C., Crenshaw D. M., Kraemer S. B., Schmitt H. R., 2013, *ApJS*, 209, 1
- Fukazawa Y. et al., 2009, *PASJ*, 61, 17
- Gandhi P., Fabian A. C., 2003, *MNRAS*, 339, 1095
- Gandhi P., Horst H., Smette A., Hönic S., Comastri A., Gilli R., Vignali C., Duschl W., 2009, *A&A*, 502, 457
- Gandhi P. et al., 2013, *ApJ*, 773, 51
- Gandhi P. et al., 2014, *ApJ*, 792, 117
- Gandhi P., Hönic S. F., Kishimoto M., 2015, *ApJ*, 812, 113
- Gehrels N. et al., 2004, *ApJ*, 611, 1005
- Gilli R., Comastri A., Hasinger G., 2007, *A&A*, 463, 79
- Gilli R. et al., 2014, *A&A*, 562, A67
- Goulding A. D., Alexander D. M., Bauer F. E., Forman W. R., Hickox R. C., Jones C., Mullaney J. R., Trichas M., 2012, *ApJ*, 755, 5
- Grossan B. A., 1992, PhD thesis, Massachusetts Institute of Technology, Cambridge
- Guainazzi M., Bianchi S., 2007, *MNRAS*, 374, 1290
- Guainazzi M. et al., 2016, *MNRAS*, 460, 1954
- Hardcastle M. J., Evans D. A., Croston J. H., 2009, *MNRAS*, 396, 1929
- Harrison F. A. et al., 2013, *ApJ*, 770, 103
- Harrison F. A. et al., 2016, *ApJ*, 831, 185
- Hönic S. F., Kishimoto M., Gandhi P., Smette A., Asmus D., Duschl W., Polletta M., Weigelt G., 2010, *A&A*, 515, A23
- Iwasawa K., Sanders D. B., Evans A. S., Mazzarella J. M., Armus L., Surace J. A., 2009, *ApJ*, 695, L103
- Iwasawa K. et al., 2012, *A&A*, 537, A86
- Kennicutt R. C., Jr 1998, *ARA&A*, 36, 189
- Kinkhabwala A. et al., 2002, *ApJ*, 575, 732
- Kokubun M. et al., 2007, *PASJ*, 59, 53
- Konami S., Matsushita K., Gandhi P., Tamagawa T., 2012, *PASJ*, 64, 117
- Koss M., Mushotzky R., Baumgartner W., Veilleux S., Tueller J., Markwardt C., Casey C. M., 2013, *ApJ*, 765, L26
- Koss M. J. et al., 2015, *ApJ*, 807, 149
- Koss M. J. et al., 2016, *ApJ*, 825, 85
- Koyama K. et al., 2007, *PASJ*, 59, 23
- Lamastra A., Bianchi S., Matt G., Perola G. C., Barcons X., Carrera F. J., 2009, *A&A*, 504, 73
- Lansbury G. B. et al., 2015, *ApJ*, 809, 115
- Lindner R. R., Baker A. J., Beelen A., Owen F. N., Polletta M., 2012, *ApJ*, 757, 3
- Liu Y., Li X., 2015, *MNRAS*, 448, L53
- Luo B. et al., 2013, *ApJ*, 772, 153
- McConnell N. J., Ma C.-P., 2013, *ApJ*, 764, 184
- Madejski G., Życki P., Done C., Valinia A., Blanco P., Rothschild R., Turek B., 2000, *ApJ*, 535, L87
- Magdziarz P., Zdziarski A. A., 1995, *MNRAS*, 273, 837
- Maiolino R., Salvati M., Bassani L., Dadina M., della Ceca R., Matt G., Risaliti G., Zamorani G., 1998, *A&A*, 338, 781
- Malaguti G. et al., 1998, *A&A*, 331, 519
- Marinucci A., Risaliti G., Wang J., Nardini E., Elvis M., Fabbiano G., Bianchi S., Matt G., 2012, *MNRAS*, 423, L6
- Marinucci A. et al., 2016, *MNRAS*, 456, L94
- Markowitz A. G., Krumpe M., Nikutta R., 2014, *MNRAS*, 439, 1403
- Mateos S. et al., 2005, *A&A*, 433, 855
- Matt G., Guainazzi M., Maiolino R., 2003, *MNRAS*, 342, 422
- Miller B. P., Brandt W. N., Schneider D. P., Gibson R. R., Steffen A. T., Wu J., 2011, *ApJ*, 726, 20
- Mineo S., Gilfanov M., Sunyaev R., 2012, *MNRAS*, 426, 1870
- Momjian E., Romney J. D., Carilli C. L., Troland T. H., 2003, *ApJ*, 597, 809
- Mullaney J. R. et al., 2015, *ApJ*, 808, 184
- Murphy K. D., Yaqoob T., 2009, *MNRAS*, 397, 1549
- Nandra K., George I. M., Mushotzky R. F., Turner T. J., Yaqoob T., 1997, *ApJ*, 488, L91
- Nandra K., O'Neill P. M., George I. M., Reeves J. N., 2007, *MNRAS*, 382, 194
- Nelson C. H., Whittle M., 1995, *ApJS*, 99, 67
- Oke J. B. et al., 1995, *PASP*, 107, 375
- Piconcelli E., Jimenez-Bailón E., Guainazzi M., Scharrel N., Rodríguez-Pascual P. M., Santos-Lleó M., 2005, *A&A*, 432, 15
- Planck Collaboration XVI, 2014, *A&A*, 571, A16
- Puccetti S. et al., 2014, *ApJ*, 793, 26
- Ranalli P., Comastri A., Setti G., 2003, *A&A*, 399, 39
- Ranalli P., Comastri A., Origlia L., Maiolino R., 2008, *MNRAS*, 386, 1464
- Ricci C., Ueda Y., Koss M. J., Trakhtenbrot B., Bauer F. E., Gandhi P., 2015, *ApJ*, 815, L13
- Ricci C. et al., 2016, *ApJ*, 820, 5
- Risaliti G., Elvis M., Fabbiano G., Baldi A., Zezas A., 2005, *ApJ*, 623, L93
- Risaliti G., Elvis M., Fabbiano G., Baldi A., Zezas A., Salvati M., 2007, *ApJ*, 659, L111
- Rivers E. et al., 2015, *ApJ*, 815, 55
- Rovilos E. et al., 2014, *MNRAS*, 438, 494
- Sako M., Kahn S. M., Paerels F., Liedahl D. A., 2000, *ApJ*, 543, L115
- Setti G., Woltjer L., 1989, *A&A*, 224, L21

- Smith R. K., Brickhouse N. S., Liedahl D. A., Raymond J. C., 2001, *ApJ*, 556, L91
 Stern D., 2015, *ApJ*, 807, 129
 Stern D. et al., 2012, *ApJ*, 753, 30
 Takahashi T. et al., 2007, *PASJ*, 59, 35
 Telesco C. M., Harper D. A., 1980, *ApJ*, 235, 392
 Treister E., Urry C. M., Virani S., 2009, *ApJ*, 696, 110
 Turner M. J. L. et al., 1989, *PASJ*, 41, 345
 Ueda Y., Akiyama M., Hasinger G., Miyaji T., Watson M. G., 2014, *ApJ*, 786, 104
 Unger S. W. et al., 1988, *MNRAS*, 234, 745
 Vasudevan R. V., Fabian A. C., 2007, *MNRAS*, 381, 1235
 Vazdekis A., Ricciardelli E., Cenarro A. J., Rivero-González J. G., Díaz-García L. A., Falcón-Barroso J., 2012, *MNRAS*, 424, 157
 Wood K. S. et al., 1984, *ApJS*, 56, 507
 Wright E. L. et al., 2010, *AJ*, 140, 1868
 Xu C., Livio M., Baum S., 1999, *AJ*, 118, 1169
 Yaqoob T., 2012, *MNRAS*, 423, 3360
 Yaqoob T., Tatum M. M., Scholtes A., Gottlieb A., Turner T. J., 2015, *MNRAS*, 454, 973

APPENDIX A:

A1 Individual *Swift* observations

A total of 17 *Swift* XRT observations of NGC 7674 are available from the HEASARC archive.⁷ Their spectra were extracted from the standard data products, and fit with simple PLs. Fixed Galactic absorption was included in these fits. In cases of insignificant detection, the gross count rate at the source position was

display an effectively hard photon index. The resultant fits are listed in Table A1. There is no evidence for significant variability amongst these measured fluxes.

A2 Model M spectral fit

Fig. A1 shows the fit to the default (coupled) Model M incorporating MYTORUS (Section 3.3). The fit parameters are listed in the last data column in Table 2. This fit is qualitatively very similar to that of Model T, shown in Fig. 3.

A3 Black hole mass estimate from optical spectroscopy

We use the penalised PiXel Fitting software (PPXF; Cappellari & Emsellem 2004) to measure the central stellar velocity dispersion (σ). For a stellar library, we used templates from the Miles Indo-U.S. Catalogue (MIUSCAT) library of stellar spectra (Vazdekis et al. 2012) with coverage of the wavelength range of the Ca II triplet (8450–8700 Å). The data and fit are presented in Fig. A2. The fit yielded a stellar velocity dispersion of $\sigma = 91 \pm 48 \text{ km s}^{-1}$ (1σ uncertainty). This value is entirely consistent with, and slightly below, the instrumental resolution $\sigma_{\text{instr.}} = 107 \text{ km s}^{-1}$. Measurements near the resolution limit can be unreliable, so we conservatively interpret the measurement and its uncertainty to be equivalent to an upper limit of $\sigma = 91 + 48 = 139 \text{ km s}^{-1}$. Using the $M_{\text{BH}}-\sigma$ relation from McConnell & Ma (2013) implies an upper limit of $M_{\text{BH}} < 10^{7.43} M_{\odot}$.

Table A1. *Swift* XRT observations of NGC 7674.

Date	ObsID	Exposure (ks)	Ct rate (10^{-3} s^{-1})	Γ	Flux ($10^{-12} \text{ erg s}^{-1} \text{ cm}^{-2}$)
(1)	(2)	(3)	(4)	(5)	(6)
2011-01-28	00040884001	1492	<20.0	1^f	< 2.15
2011-10-03	00040884002	845	<13.8	1^f	< 1.49
2011-10-04	00040884003	845	<26.7	1^f	< 2.87
2011-10-28	00040884004	4952	5.9 ± 1.9	$-1.52_{-u}^{+1.55}$	$2.13_{-1.09}^{+1.96}$
2011-10-30	00040884005	3696	7.9 ± 2.7	$-0.23_{-1.16}^{+1.20}$	$1.46_{-0.66}^{+1.11}$
2011-11-03	00040884006	2831	9.2 ± 3.2	$-0.46_{-1.68}^{+1.76}$	$1.63_{-0.92}^{+1.16}$
2011-11-08	00040884007	2782	4.3 ± 2.2	$-1.11 \pm u$	$1.46_{-1.01}^{+3.01}$
2011-11-11	00040884008	4701	5.1 ± 1.9	$3.15_{-2.58}^{+3.00}$	$0.94_{-0.36}^{+1.42}$
2011-11-13	00040884009	4997	5.8 ± 1.9	$-0.03_{-1.32}^{+1.31}$	$0.98_{-0.45}^{+0.85}$
2011-11-15	00040884010	3929	4.4 ± 1.9	$-1.88_{-u}^{+2.21}$	$2.40_{-1.60}^{+2.55}$
2011-11-17	00040884011	467	<25.4	1^f	< 2.73
2011-11-19	00040884012	5077	4.0 ± 1.6	$-0.11_{-2.67}^{+2.70}$	$0.99_{-0.48}^{+1.5}$
2011-11-21	00040884013	4679	3.8 ± 1.6	$0.46_{-1.90}^{+1.84}$	$0.94_{-0.44}^{+1.15}$
2013-01-29	00049851001	1454	<9.5	1^f	< 1.02
2014-09-30	00080798001	1041	<21.7	1^f	< 2.34
2014-10-03	00080798002	3078	<9.1	1^f	< 0.98
2014-10-08	00080798003	2395	7.4 ± 3.0	$0.55_{-1.86}^{+1.79}$	$0.92_{-0.53}^{+1.59}$

Notes. Ct rates (3), fitted Γ (4) and flux (5) are for the 2–10 keV range where the AGN is expected to dominate.

^ffixed photon indices used for flux upper limit determinations.

^uunconstrained.

converted to an upper limit on the observed flux assuming a PL of fixed $\Gamma = 1$ because we expect the source to be obscured and

⁷ <http://heasarc.gsfc.nasa.gov/docs/archive.html>

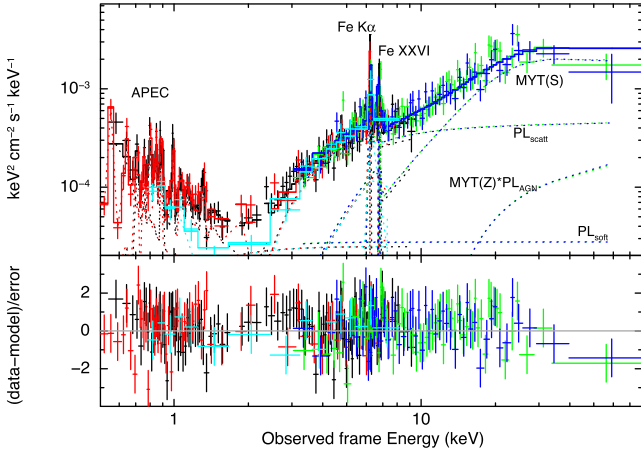


Figure A1. *Suzaku* + *NuSTAR* data fits with the reflection Model M. This is very similar to Model T presented in Fig. 3. The MYT(z) and MYT(s) components represent the absorption of the direct component, and the Compton-scattered component, respectively. The third MYTORUS component is the fluorescence component producing the Fe $K\alpha$ and related emission features and the Compton shoulders (this would be equivalently named MYTL).

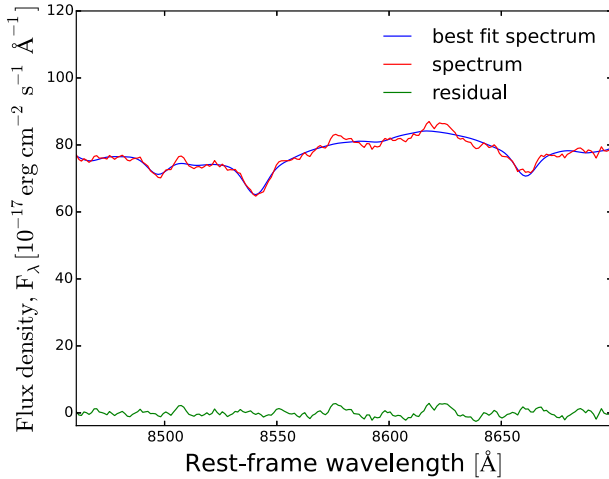


Figure A2. Keck/LRIS red grism spectrum of NGC 7674 spanning the Ca II triplet absorption feature, fitted with a PPF algorithm. The intrinsic velocity dispersion is measured to be $91 \pm 48 \text{ km s}^{-1}$.

The measurement quoted by Nelson & Whittle (1995) is $\sigma = 144 \pm 32 \text{ km s}^{-1}$, which has been used to infer $M_{\text{BH}} = 10^{7.56} M_{\odot}$ in the literature (Bian & Gu 2007). Nelson & Whittle used the KPNO 2.1-m telescope with the TI CCD, a slit width of 1.5 arcsec, and 600 lines mm^{-1} grating, observed under 1.9 arcsec seeing. The grating would have had higher spectral resolution than our LRIS observations, so it is a bit surprising that their measurement of σ is larger than our inferred upper limit.

However, we note that the uncertainty of 32 km s^{-1} suggests that the discrepancy is relatively mild. Their use of a wider slit, the bad seeing during their observation, and use of a far smaller telescope than Keck may have all resulted in lower signal-to-noise ratio than our data. In fact, a comparison by eye of our Fig. A2 with the spectrum presented in Fig. 3a of Nelson & Whittle (1995) shows this to be a plausible solution to the above mismatch. A sensitive, higher resolution optical spectrum, with 1200 lines mm^{-1} , for instance, should be able to resolve this issue.

¹Department of Physics and Astronomy, University of Southampton, Highfield, Southampton SO17 1BJ, UK

²Centre for Extragalactic Astronomy, Department of Physics, Durham University, South Road, Durham DH1 3LE, UK

³Institute of Astronomy, University of Cambridge, Madingley Road, Cambridge CB3 0HA, UK

⁴Jet Propulsion Laboratory, California Institute of Technology, 4800 Oak Grove Drive, Mail Stop 169-221, Pasadena, CA 91109, USA

⁵Instituto de Astrofísica and Centro de Astroingeniería, Facultad de Física, Pontificia Universidad Católica de Chile, Casilla 306, Santiago 22, Chile

⁶Millennium Institute of Astrophysics (MAS), Nuncio Monseñor Sótero Sanz 100, Providencia, Santiago, Chile

⁷Space Science Institute, 4750 Walnut Street, Suite 205, Boulder, Colorado 80301, USA

⁸Dipartimento di Matematica e Fisica, Università degli Studi Roma Tre, via della Vasca Navale 84, I-00146 Roma, Italy

⁹Space Sciences Laboratory, University of California, Berkeley, CA 94720, USA

¹⁰Department of Astronomy and Astrophysics, 525 Davey Lab, The Pennsylvania State University, University Park, PA 16802, USA

¹¹Institute for Gravitation and the Cosmos, The Pennsylvania State University, University Park, PA 16802, USA

¹²Department of Physics, Pennsylvania State University, University Park, PA 16802, USA

¹³Cahill Center for Astrophysics, 1216 East California, Boulevard, California Institute of Technology, Pasadena, CA 91125, USA

¹⁴DTU Space-National Space Institute, Technical University of Denmark, Elektrovej 327, DK-2800 Lyngby, Denmark

¹⁵INAF Osservatorio Astronomico di Bologna via Ranzani 1, I-40127 Bologna, Italy

¹⁶Lawrence Livermore National Laboratory, Livermore, CA 94550, USA

¹⁷Max-Planck-Institut für Extraterrestrische Physik (MPE), Postfach 1312, D-85741 Garching, Germany

¹⁸Harvard-Smithsonian Center for Astrophysics, 60 Garden Street, Cambridge, MA 02138, USA

¹⁹Institute of Space and Astronautical Science (JAXA), 3-1-1 Yoshinodai, Sagami-hara, Kanagawa, 252-5252, Japan

²⁰European Space Astronomy Center of ESA, PO Box 78, Villanueva de la Cañada, E-28691 Madrid, Spain

²¹Columbia Astrophysics Laboratory, 550 W 120th Street, Columbia University, NY 10027, USA

²²Institute for Astronomy, Department of Physics, ETH Zurich, Wolfgang-Pauli-Strasse 27, CH-8093 Zurich, Switzerland

²³INAF Istituto di Astrofisica Spaziale e Fisica cosmica di Bologna, via Gobetti 101, I-40129 Bologna, Italy

²⁴Dipartimento di Fisica e Astronomia (DIFA), Università di Bologna, viale Bertini Pichat 6/2, I-40127 Bologna, Italy

²⁵ASDC-ASI, Via del Politecnico, I-00133 Roma, Italy

²⁶INAF-Osservatorio Astronomico di Roma, via Frascati 33, I-00040 Monte Porzio Catone (RM), Italy

²⁷X-ray Astrophysics Laboratory, NASA Goddard Space Flight Center, Greenbelt, MD 20771, USA